



**HAL**  
open science

## A phase inversion benchmark for multiscale multiphase flows

Stéphane Vincent, Ludovic Osmar, Jean-Luc Estivalezes, Stéphane Zaleski, Franck Auguste, W. Aniszewski, Yue Ling, Thibaut Ménard, Annaig Pedrono, Jacques Magnaudet, et al.

► **To cite this version:**

Stéphane Vincent, Ludovic Osmar, Jean-Luc Estivalezes, Stéphane Zaleski, Franck Auguste, et al.. A phase inversion benchmark for multiscale multiphase flows. 2020. hal-03419715v1

**HAL Id: hal-03419715**

**<https://hal.science/hal-03419715v1>**

Preprint submitted on 4 Jun 2020 (v1), last revised 8 Jan 2024 (v2)

**HAL** is a multi-disciplinary open access archive for the deposit and dissemination of scientific research documents, whether they are published or not. The documents may come from teaching and research institutions in France or abroad, or from public or private research centers.

L'archive ouverte pluridisciplinaire **HAL**, est destinée au dépôt et à la diffusion de documents scientifiques de niveau recherche, publiés ou non, émanant des établissements d'enseignement et de recherche français ou étrangers, des laboratoires publics ou privés.

# A phase inversion benchmark for multiscale multiphase flows

S. Vincent<sup>§,†,a</sup>, L. Osmar<sup>†</sup>, J.-L. Estivalezes<sup>♣</sup>, S. Zaleski<sup>+</sup>,  
F. Auguste<sup>°,∇</sup>, W. Aniszewski<sup>\*,+</sup>, Y. Ling<sup>+,b</sup>, T. Ménard<sup>\*</sup>,  
A. Pedrono<sup>°</sup>, J. Magnaudet<sup>°</sup>, J.-P. Caltagirone<sup>†</sup>,  
A. Berlemont<sup>\*</sup>, S. Popinet<sup>+</sup>

<sup>a</sup>*stephane.vincent@u-pem.fr (corresponding author)*

<sup>§</sup> Université Paris-Est Marne-La-Vallée and CNRS, Laboratoire  
Modélisation et Simulation Multi Echelle (MSME), UMR 8208, F-77454,  
Marne-La-Vallée, France

<sup>†</sup> Université de Bordeaux and CNRS, Institut de Mécanique et Ingénierie  
(I2M), UMR 5295, F-33607 Pessac, France

<sup>°</sup> Université de Toulouse and CNRS, Institut de Mécanique des Fluides de  
Toulouse (IMFT), UMR 5502, F-31400 Toulouse, France

<sup>+</sup> Sorbonne Université and CNRS, Institut Jean Le Rond d’Alembert,  
UMR 7190, F-75005 Paris, France

<sup>\*</sup> Université de Rouen and CNRS, Complexe de Recherche  
Interprofessionnel en Aérothermochimie (CORIA), UMR 6614, F-76801  
Saint-Etienne-du-Rouvray Cedex, France

<sup>b</sup> Baylor University, Department of Mechanical Engineering, Waco, TX  
76706, USA

<sup>♣</sup> ONERA, The French Aerospace Lab, F-31055 Toulouse, France

<sup>∇</sup> CERFACS, Centre Européen de Recherche et de Formation Avancée en  
Calcul Scientifique, F-31057 Toulouse, France

## Abstract

A series of benchmarks based on the physical situation of “phase inversion” between two incompressible liquids is presented. These benchmarks aim at progressing toward the direct numerical simulation of two-phase flows. Several CFD codes developed in French laboratories and using either Volume of Fluid or Level Set interface tracking methods are utilized to provide physical solutions of the benchmarks, convergence studies and code comparisons. Two typical configurations are retained, with integral scale Reynolds numbers of  $1.37 \cdot 10^4$  and  $4.33 \cdot 10^5$ , respectively. The physics of the problem are probed through macroscopic quantities such as potential and kinetic energies, interfacial area, enstrophy or volume ratio of the light fluid in the top part

of the cavity. In addition, scaling laws for the temporal decay of the kinetic energy are derived to check the physical relevance of the simulations. Finally the droplet size distribution is probed. Additional test problems are also reported to estimate the influence of viscous effects in the vicinity of the interface.

**keywords:** phase inversion, multiphase flows, benchmark, Volume Of fluid, Level Set, Ghost Fluid

# 1 Introduction

The physical validation or verification of CFD tools devoted to multiphase flows and non miscible fluids, (by non-miscible we mean that interfaces remain sharp), is a major concern. A lot of work was carried out in the 90s to validate interface tracking algorithms in cases where the velocity field is given analytically [1] [2]. Comparisons have also been achieved with available experiments or predictions of linear stability theories [3]. However, in almost all of these situations, the topology of the interface is rather simple and the flow problem lies in a single multiphase characteristics such as the continuity of stresses across the interface with the two-phase Poiseuille flow [4], the Laplace law [5], the oscillation modes of a free surface [6] [5], the head-on coalescence of two drops [7] [8], the dam break problem [9] or the break-up of a low-velocity round jet due to the Rayleigh-Plateau instability [10] to mention just a few.

None of these problems puts into play the interaction between interfaces and turbulence or unsteady flows which is a key point in many realistic cases involving a two-phase dynamics. Indeed, such multiphase interactions occur in many environmental and industrial applications. Let us just mention the atomization of a liquid jet in an engine [11–13], phase separators in chemical engineering processes, the boiling crisis in nuclear reactors [14], complex bubble flow including the flow past Taylor bubbles in pipes [15], droplet or asteroid impact [16], wave impact on structures or the ubiquitous phenomenon of wave breaking at the ocean surface [17]. In most multiphase flows of environmental or engineering relevance, the multiscale character of the flow is a key issue to be handled by computational approaches. The interfacial length scales are associated on the one hand to large interface structures such as jets, films or large drops. On the other hand, small interfacial scales also exist, corresponding to a small-scale dispersed phase, *i.e.* small bubbles or droplets. These two widely distinct families of interfacial scales interact in a nonlinear way through ligament break-up or drop/bubble coalescence and the unsteady or turbulent nature of the carrier fluid motion plays a crucial role in these interactions. The definition of a reference benchmark for these multiscale sharp interface problems appears to be an important issue.

Homogeneous Isotropic Turbulence (HIT) often serves as a reference problem in the verification of single-phase DNS codes. In analogy, one would like to define a reference problem for the verification of CFD multiphase flow codes devoted to non miscible fluids. Our first idea was to try to define the reference problem on the basis of a well documented experiment, such

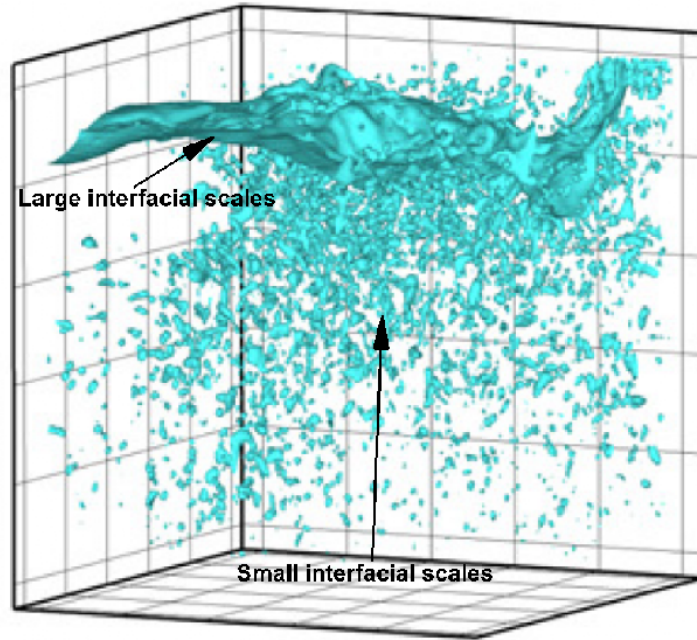


Figure 1: Example of simulated phase inversion in a closed box [18] illustrating the multiscale character of the interfacial flow.

as atomization of liquid sheets or jets. However, the quality of modeling and simulation of atomization is very sensitive to inlet forcing conditions, in particular due to upstream turbulence, boundary layers or inlet pump oscillations [19, 20]. Although numerous experimental studies can be found in the literature [9, 21, 22] they are plagued by two difficulties that make them unsuitable as reference cases: either they have too simple flow structures (as for dam break on a dry bottom) or they are not sufficiently well documented or instrumented to provide all the information required for defining boundary and initial conditions for simulations. Moreover many experiments lack instantaneous pressure, velocity and interface measurements (dam break on a wet bottom [23]). As a consequence, we have decided to define a synthetic reference case unrelated to a specific experiment, although an experiment in this configuration could in principle be considered (the setup resembles that of an oil and water phase separator or settling pond). In this reference case initial and boundary conditions are simple and well known. At the same time, we wish to have complex flow features (turbulence, interface rupture, coalescence, multi-scale flow characteristics). A setup we believe satisfies all these requirements is a cubic outer geometry and a simple arrangement of the

phases both as initial condition and final equilibrium state of the dynamics, so that grid quality and its influence on the Navier-Stokes solver performance will not be a problem. At the same time, there are advantages to consider sufficiently large Reynolds number  $Re$  and Weber number  $We$  to have the multiphase equivalent of “fully developed turbulence”, a state in which the statistical features of the flow on large and intermediate scales become relatively independent of  $Re$  and  $We$  as those numbers further increase. Such fully developed multiphase turbulence is the relevant flow state with respect to common natural sciences or engineering situations.

The simple cubic geometry idea leads naturally to the phase inversion of a cube of light fluid inside a larger cube of a heavier fluid contained in a closed box. As desired, with high enough  $Re$  and  $We$  this flow configuration is typical of fully developed turbulent multiscale flows in which a broad range of interfacial scales (*i.e.* those characterizing the typical size of the interfaces separating the two fluids) coexist: as a result of multiple break-up and coalescence events, large-scale sloshing motions are observed together with small dispersed droplets interacting with larger drops. An illustration is given in Figure 1 taken from [18], [24]. As described in Figure 2, the initial condition is geometrically straightforward and the solution at large times is known, *i.e.* in the final stage the two fluids are superimposed in a stable manner (with all the light fluid in the top part of the box) and are separated by a single horizontal interface. A parametric study in which various physical parameters are varied can easily be performed by changing the density or viscosity ratios as well as the surface tension. From a numerical point of view, the physical parameters can be defined in such a way that a numerical convergence study may be achieved until a true direct numerical simulation (DNS) is obtained, *i.e.* all the flow and interfacial time and space scales are resolved. The sensitivity of the results with respect to the grid density or to the numerical methods can also be examined. Laminar as well as turbulent conditions can be generated. Regimes corresponding to either thinly dispersed flows or to large-drop topologies can be selected by properly choosing the physical characteristics of the two fluids.

Among the wide number of references existing on the subject of multiphase flow modeling and simulation, it appears to us that there are two categories of work, those concerning mixing and diffuse evolution of initially discontinuous distribution of fluids and those associated to interfaces remaining sharp during time, *i.e.* immiscible fluids. The first category has investigated for example the interaction between Rayleigh-Taylor (RT) instabilities and turbulence in numerous works [25–28] and a benchmark has been published in

2004 by Dimonte and co-workers [29]. This reference work involves physical phenomena similar to those occurring in the phase inversion configuration proposed here. Much attention has been paid to characterizing, with various models and numerical methods, the effects of initial perturbations of the interface, volume fraction profiles, self-similar bubble dynamics or mixing behavior. However, the major difference is related to the immiscible nature of fluids and discontinuous character of interface (on a macroscopic point of view). It has been clearly demonstrated [28] that the diffuse character of the fluids has a major effect on the global dynamics of the turbulent two-phase flow in terms of spike position for example and that this discrepancy was increasing during time. In diffuse modeling of RT flows, simulations mainly involve gas stratifications whereas our focus here is on immiscible fluids (with at least to one liquid phase in the considered problem). Our benchmark thus belongs to the second category of problems for which RT simulations also exist [30, 31]. Intermediate modeling between diffuse and sharp interfaces have also been proposed for simulating Rayleigh-Taylor instabilities [32]. The major concern was the model and numerical methods and there was no consideration of the turbulence characteristics of the flows. To our knowledge, neither benchmark nor detailed simulation works have been published about RT interaction with turbulence in the framework of sharp liquid interfaces and immiscible fluids. In that sense, the present work is a relevant and new contribution for the CFD community of multiphase flows with sharp interfaces.

The convergence study is the first original outcome of this work. Indeed, neither detailed nor accurate experimental measurements seem to exist for the phase inversion problem considered here. Therefore it is of fundamental interest to validate the quality of the various technical s.png of the computations, namely the numerical schemes, the Navier-Stokes solvers, etc. Our second objective is to determine whether or not the interface tracking techniques and the numerical methods required to discretize the two-phase Navier-Stokes equations (*e.g.* the definition of the two-phase viscosity as a function of those of the two fluids) can provide consistent solutions for the multiphase and multiscale flow problem at hand. To meet both objectives, a comparison of the performance of five distinct in-house DNS multiphase flow codes on the reference or benchmark case is provided in what follows. It highlights the capabilities but also the limitations of up-to-date numerical methods and interface models to tackle multiscale, multiphase, flow problems.

## 2 Definition of the phase inversion benchmark

The phase inversion configuration has previously been proposed or used [33] without the objective of analyzing the physical aspects of the multiscale character of the flow, nor comparing various interface tracking methods. A benchmark based on this flow situation was also recently performed using VOF methods [31]. The simulation of this configuration was used to obtain *a priori* estimates of subgrid terms that appear and must be modeled when LES is used in the framework of two-phase flows of immiscible fluids [34]. A new selection of the physical parameters is achieved here (see Tables 1,2 and 3). With the very high Re and La numbers achieved (Table 3) viscosity is considerably smaller than what would be needed to obtain fully-resolved simulations in multiphase as well as in single phase flow. (Note that other computations were performed in [35] [33] [18] [24].) The two cases that are presented in this work are a good illustration of an atomization process at large Reynolds number. We cannot hope to perform a Direct Numerical Simulation in the sense of a simulation with all length scales resolved. Clearly, our simulations without explicit turbulent or subgrid droplet modeling, are finely-resolved implicit Large Eddy Simulations.

### 2.1 Geometry, initial and boundary conditions

As described in Figure 2, an initial cubic blob of light liquid, referred to as fluid 1, is placed in the bottom part of a cubic box filled with a heavier liquid, referred to as fluid 2. The size of the box is  $(H, H, H)$ , while the size of the blob of light fluid is  $(H/2, H/2, H/2)$ . All outer walls are considered as free-slip impermeable walls, so that the normal velocity is zero and the tangential components obey a symmetry condition. A  $\pi/2$  static contact angle is implicitly assumed on the walls. Gravitational acceleration is chosen as  $\mathbf{g} = (0, -9.81, 0)$ . Besides the simplicity of the initial and final configurations of the phase inversion problem, another of its advantages is that it provides the possibility to observe multiple coalescence and break-up events, although that introduces an additional complexity since in a simulation coalescence is conditioned by numerical rather than physical properties. In this setup we may conveniently observe fragmentation of ligaments in a kind of atomization process, while not depending on complex initial or forcing conditions such as those encountered in real atomization configurations [36], [37]. The main disadvantage of this benchmark case is that no experimental data are available.

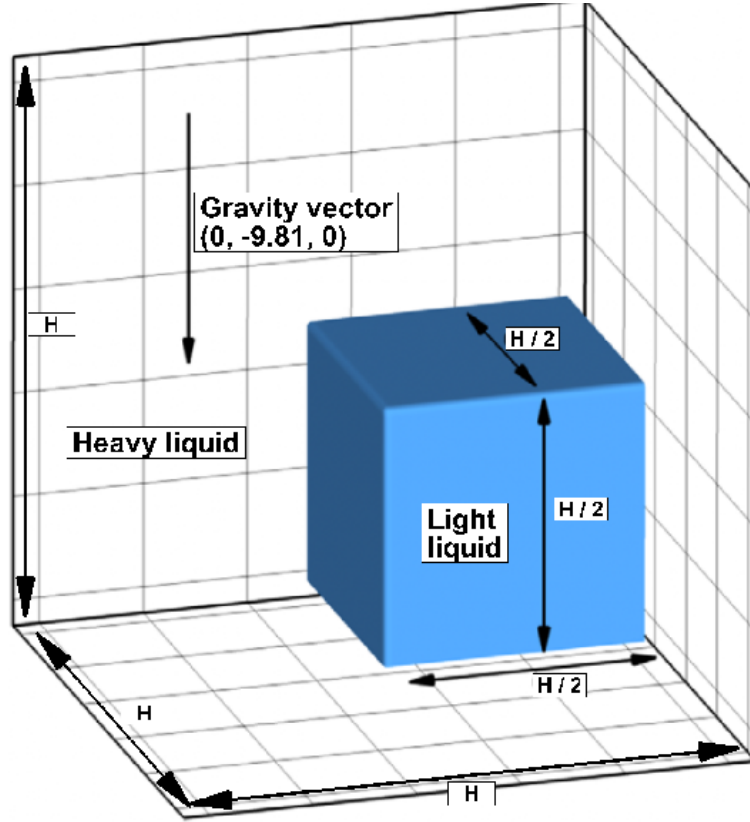


Figure 2: Sketch of the phase inversion problem in a closed box.

## 2.2 Physical parameters of the test cases

Characteristics of the fluids are varied in order to investigate various multiscale interface topologies. The fluid properties control these conditions, which may be expressed in terms of  $Re$ , and  $We$ . In order to define these numbers we need to define a velocity scale. We obtain it from energy considerations. In all of what follows, we use the characteristic or color function  $C$  that is defined with respect to fluid 1, so that  $C = 1$  in fluid 1 and  $C = 0$  in fluid 2. The potential energy of phase  $n$  is

$$E_{p,n} = \int_{\Omega} C_n \rho_n g y dV \quad (1)$$

where  $C_k$  is the characteristic function of phase  $n$ :  $C_1 = C$ ,  $C_2 = 1 - C$  and with  $g = \|\mathbf{g}\|$ . The kinetic energy of phase  $n$  is

$$E_{k,n} = \frac{1}{2} \int_{\Omega} C_n \rho_n \mathbf{u}^2 dV \quad (2)$$

Due to the simple topology of the interface in the initial and final s.png the potential energies are trivially found. At  $t = 0$ ,  $E_{p,1}^i = \rho_1 g H^4 / 32$  and  $E_{p,2}^i = 15 \rho_2 g H^4 / 32$  while for  $t \rightarrow \infty$ ,  $E_{p,1}^f = 15 \rho_1 g H^4 / 128$  and  $E_{p,2}^f = 49 \rho_2 g H^4 / 128$ . An upper bound on the kinetic energy is

$$E_{k,1} + E_{k,2} \leq E_{p,1}^i + E_{p,2}^i - E_{p,1}^f - E_{p,2}^f = \frac{11}{128} (\rho_2 - \rho_1) g H^4 \quad (3)$$

and an upper bound on the velocity is  $\|\mathbf{u}\|_2 < (2E_k/\rho_1)^{1/2}$ . Identifying the velocity with the upperbound we obtain the velocity scale

$$U_K = \frac{\sqrt{11}}{8} \sqrt{\frac{\rho_2 - \rho_1}{\rho_1} g H}$$

The dimensionless numbers are defined based on  $U_K$  and properties of fluid 2,

$$\text{Re} = \frac{\rho_2 H U_K}{\mu_2}, \quad (4)$$

$$\text{We} = \frac{\rho_2 H U_K^2}{\sigma}, \quad (5)$$

As is customary in atomization problems, the Reynolds and Weber numbers may be combined in a way that eliminates the velocity scale, yielding the Laplace number  $\text{La} = \sigma \rho_2 H / \mu_2^2 = \text{Re}^2 / \text{We}$ .

To allow comparison with previous work on this setup we also define the same velocity scale as in previous studies by some of us [18, 24, 34]  $U_g = \frac{\rho_2 - \rho_1}{\rho_1} \sqrt{\frac{H g}{2}}$  and a characteristic time scale  $t_c = H / (2U_g)$ .

The fluid properties correspond approximately to oil (fluid 1) and water (fluid 2). These configurations are interesting in so far as they provide interface and turbulent characteristics similar to those of jet atomization with simpler and more easily controlled initial conditions, and are as a result more convenient for numerical simulations. These liquid-liquid two-phase flows make it possible to select easily a range of Reynolds numbers smaller, or even equivalent, to those encountered in real atomization processes while exhibiting equivalent dynamics. The characteristics of fluid 1 and related dimensionless numbers are given in Tables 1,2 and 3. Case 1 corresponds to a configuration with moderate fragmentation. Case 2 has increased size and thus larger Reynolds number (by a factor of 30 compared to case 1). The Weber number is also higher in case 2, (by a factor of 10 compared to case 1) but does not grow as rapidly as the Reynolds number since surface tension was also

artificially increased. This was done specifically to avoid having an exceedingly large Weber number which would lead to excessive fragmentation of the interface. Nevertheless both cases involve large inertial effects and low capillary forces resulting in the generation of a large number of droplets.

$\rho_1$	$\rho_2$	$\mu_1$	$\mu_2$	$g$
$(kg.m^{-3})$	$(kg.m^{-3})$	$(Pa.s)$	$(Pa.s)$	$(m.s^{-2})$
900	1000	0.1	0.001	9.81

Table 1: Common fluid and physical properties

Case	$\sigma$	$H$
	$(kg.s^{-2})$	$(m)$
1	0.045	0.1
2	0.45	1

Table 2: Fluid and physical properties that depend on the case considered.

Case	Re	We	La=Re <sup>2</sup> /We
1	$1.37 \cdot 10^4$	41.6	$4.5 \cdot 10^6$
2	$4.33 \cdot 10^5$	416	$4.5 \cdot 10^8$

Table 3: Dimensionless numbers for the cases considered.

## 2.3 Macroscopic quantities of interest

Several macroscopic quantities characterizing the evolution of the flow field are of primary interest. Among these physically relevant quantities we select the following.

- A measure of the amount of fluid 1 that has reached the upper part of the box. The upper part is the box  $\Omega_{up}$  of dimension  $(H, H, H_2)$  at the top of domain. As  $t \rightarrow \infty$  it is the exact location of fluid 1. Given the initial volume of fluid 1, we have  $H_2 = H/8$  and the ratio

$$R_2 = \frac{1}{V_2} \int_{\Omega_{up}} C_2 dV \quad (6)$$

is a relevant quantitative representation of the phase separation process which has the asymptotic value  $R_2 = 1$ . In the benchmark, values of (6) will be saved at each time step of the simulations. Their evolution will help us estimate the typical time of phase separation time and characterize the macroscopic dynamics of the problem.

- The potential and kinetic energies will be stored at each time step. They will help monitor the conversion of potential energy into kinetic energy and provides a characterization of the density stratification.
- The time evolution of the volume integral of the enstrophy in both fluids will also be recorded. This quantity is defined as  $E_{r,n} = \int_{\Omega} C_n \mathbf{w}^2 dV/2$ , with  $\mathbf{w} = \nabla \times \mathbf{u}$  denoting the vorticity.
- The time evolution of the interfacial area will also be recorded, being a sensitive marker of grid convergence. This parameter is also relevant in problems involving interfacial energy or mass transfer [38], [39]. To estimate it, we introduce a binary presence function  $C^b$  such that  $C^b = 0$  if  $C < 0.5$  and  $C^b = 1$  elsewhere. This function can also be easily built from the level set function. The interfacial area  $\Sigma_{int}$  is finally approximated as

$$\Sigma_{int} \approx \sum_{\{i,j,k: \|\nabla C_{i,j,k}^b\| \neq 0\}} \Delta x \Delta y. \quad (7)$$

### 3 Model and numerical methods

As is now well established, incompressible two-phase flows involving fluid-fluid interfaces and Newtonian fluids can be modeled by a single set of incompressible Navier-Stokes equations with phase-specific density and viscosity and possibly extra interfacial forces (*e.g.* the capillary force), together with the transport equation of the phase function  $C$ . The resulting model takes implicitly into account the mass and momentum jump relations at the interface [40] [41], whereas the continuity of the fluid-fluid and fluid-solid interfaces are taken into account by the  $C$  equation. The entire set of equations reads:

$$\nabla \cdot \mathbf{u} = 0, \quad (8)$$

$$\rho \left[ \frac{\partial \mathbf{u}}{\partial t} + (\mathbf{u} \cdot \nabla) \mathbf{u} \right] = -\nabla p + \rho \mathbf{g} + \nabla \cdot [\mu (\nabla \mathbf{u} + \nabla \mathbf{u}^T)] + \mathbf{F}_{st}, \quad (9)$$

$$\frac{\partial C}{\partial t} + \mathbf{u} \cdot \nabla C = 0, \quad (10)$$

where  $p$  is the pressure,  $\mathbf{F}_{st}$  is the interfacial force per unit volume and  $\rho$  and  $\mu$  are the local density and viscosity of the two-phase medium, respectively.

Capillary effects are inserted in the source term  $\mathbf{F}_{st}$  in the form  $\mathbf{F}_{st} = \sigma \kappa \mathbf{n}_i \delta_i$ , where  $\sigma$  denotes the surface tension,  $\kappa$  is the local mean curvature of the interface,  $\mathbf{n}_i$  is the unit vector normal to the interface and  $\delta_i$  is the interface Dirac function [42].

The above one-fluid model is the classical model for multiphase incompressible flow with sharp interfaces and surface tension. Localizing the interface requires solving the additional transport equation for the characteristic function  $C$ . This can be performed using the volume fraction (also noted  $C$  in Volume-of-Fluid methods) or using a continuous level-set function  $\phi$  such that  $\phi = 0$  at the interface and  $\phi > 0$  (resp.  $< 0$ ) in fluid 2 (resp. 1). In this case, the characteristic function is obtained as  $C = H(\phi)$  where  $H$  is the Heaviside function [43].

Note that the above equations are clearly distinct from those appearing in various models of single or multiphase turbulence, that may involve Reynolds stresses, terms for unresolved eddies or turbulent viscosities and diffusivities, and non-sharp interfaces.

### 3.1 The Thétis code

Thétis is a CFD code developed in the TREFLE Department of the I2M laboratory. It solves the one-fluid Navier-Stokes equations discretized with implicit finite-volumes on an irregular staggered Cartesian grid. A second-order centered scheme is used to approximate the spatial derivatives while a second-order Euler or Gear scheme is used for the time integration [44]. All terms are written at time  $(n + 1)\Delta t$ , except the inertial term which is expressed in the following semi-implicit manner:

$$\mathbf{u}^{n+1} \cdot \nabla \mathbf{u}^{n+1} \approx (2\mathbf{u}^n - \mathbf{u}^{n-1}) \cdot \nabla \mathbf{u}^{n+1}. \quad (11)$$

It has been shown that this approximation allows to reach second-order convergence in time [45]. The coupling between velocity and pressure is ensured by using an implicit algebraic adaptive augmented Lagrangian method [46]. The augmented Lagrangian methods used in this work are independent on the chosen discretization and could for instance be implemented in a finite-element framework [47]. In two dimensions, the standard augmented Lagrangian approach [48] can be used to deal with two-phase flows as direct

solvers [49] are efficient in this case. However, as soon as three-dimensional problems are considered, the linear system resulting from the discretization of the augmented Lagrangian terms has to be treated with a BiCG-Stab II solver, preconditioned by a Modified and Incomplete LU method [50]. As for the interface tracking and advection equation of  $C$ , two different volume of fluid (VOF) methods have been implemented in Thétis [51] [52]. They are evaluated here. The above numerical methods and the one-fluid model have been validated in previous works, *e.g.* [53] and [54].

### 3.2 The Gerris Flow Solver code

The Gerris Flow Solver (GFS) is a free code implementing finite volume solvers on an octree adaptive grid together with a piecewise linear VOF interface-tracking method. In this work, the Navier-Stokes equations for an incompressible two-phase flow with constant surface tension are solved. The simulations reported in this paper use a VOF method of the piecewise linear type, in which the interface segments are reconstructed using the mixed-Youngs-centered (MYC) approximation [55]. While not the most accurate for very fine grids, the MYC approximation is easily implemented when using only information from the nearest-neighbour cells, an important advantage when domain-decomposition on octrees is used. Advection of  $C$  is performed using the Lagrangian-Explicit method first published by Li [56] and discussed in [57–59]. While not volume-conserving to machine accuracy, it has very good volume and mass conservation properties. Surface tension is a vexing question in multiphase flow. As density and viscosity ratios become very large or very small, the simulations become increasingly difficult with standard methods [59]. The problem has been considerably improved in Gerris as a result of the use of Height-Function methods [5] and a so-called balanced-force algorithm [60, 61]. For a review of surface-tension methods including a discussion of the differences between those used in Gerris and in other codes, see [62]. Gerris has been used with success in two-dimensional [63] and three-dimensional [64, 65] atomization and droplet impact studies.

### 3.3 The Jadim code

JADIM is a versatile code developed for a number of years at IMFT (Institut de Mécanique des Fluides de Toulouse). In JADIM, the time evolution of two-phase or three-phase flow is obtained using the one-fluid formulation of the Navier-Stokes equations. The momentum equations are discretized on a stag-

gered orthogonal grid using a finite-volume approach. Spatial discretization is performed using second-order centered differences. Time-advancement is achieved through a third-order Runge-Kutta algorithm for advection/source terms and a Crank-Nicolson algorithm for viscous stresses. Incompressibility is satisfied at the end of each time step through a projection method. More details may be found in [38]. The resulting code is second-order accurate in both time and space for single-phase flows.

In two- and three-phase configurations, a VOF method with no interface reconstruction is used. The advection equation for  $C$  is solved using a flux-corrected scheme split into successive one-dimensional s.png [66]. Owing to the splitting procedure, the overall transport scheme is not rigorously conservative. Therefore a local mass error control which improves upon the global control technique described in [56] is employed. The corresponding strategy is based on the detection of drop or bubbles (through an index function and a topological monitoring of each bubble or drop) and on an iterative solution which modifies the volume fraction within the transition regions (i.e. those in which the volume fraction is neither zero nor one) in order to keep the volume of each bubble or drop constant. Since no interface reconstruction step is involved, smearing of interfaces frequently occurs in high-shear regions. A specific strategy is employed to keep this smearing within reasonable bounds. For this purpose, the velocity at nodes crossed by the interface is modified to keep the thickness of the interfacial region constant. Details may be found in [4, 66]. In the most difficult cases (e.g. break-up and coalescence), this approach is supplemented by an antidiffusion technique in which the local volume is redistributed in the direction normal to the interface so as to eliminate spurious values of the volume fraction outside interfacial regions.

The capillary force is represented using a modified version of the Continuum Surface Force (CSF) model [42]. The modification used in JADIM consists in an original manner of evaluating the interfacial area. It allows us to define the interfacial region as that in which the capillary force takes non-zero values (not as that in which the volume fraction takes intermediate values) and improves the control of the thickness of the transition region.

### 3.4 The Archer code

Archer is a CFD code developed in the CORIA Laboratory mainly devoted to multiphase flows. It has been previously applied to compute atomization [36],

vaporization and mixing [67] and other complex interfacial flows [31]. The Level Set (LS) method [43] is used for tracking interfaces and shapes. It is based on a continuous distance function  $\phi$  defined as the signed distance between any point of the domain and the interface. Similar to the volume fraction  $C$ ,  $\phi$  obeys a pure advection equation.

To avoid singularities in the  $\phi$  field, the fifth order conservative WENO [68] scheme is applied to discretize convective terms. When the LS advection is carried out, high velocity gradients can cause wide spreading or stretching of  $\phi$  which then no longer remains a distance function. A redistancing algorithm [69] is thus applied at every time step to restore the distance property of  $\phi$ , *i.e.*  $|\nabla\phi| = 1$ . Advancement of the  $\phi$ -equation and the redistancing algorithm can induce mass loss in under-resolved regions [31]. This is the main drawback of Level Set methods. To improve mass conservation, the Coupled Level-Set Volume of Fluid (CLSVOF) method [70] is used. The main idea of this method is to benefit from the advantages of each tracking strategy: minimize the mass loss using VOF and keep a fine description of interface properties with the smooth LS function. (A study of the performance of various VOF variants was recently published [31] using Archer in the CLSVOF context; the phase inversion problem is also discussed therein.) The coupling between LS and VOF is maintained using a correction scheme based on geometric reconstruction of both VOF and LS interfaces [34]. The LS method itself is coupled with a projection method for the incompressible Navier–Stokes equations, where the density and the viscosity depend on the sign of the LS function (with appropriate interpolations used in interfacial cells). To finalize the description of the two-phase flow, jump conditions across the interface are taken into account using the Ghost Fluid (GF) method. In the GF approach, ghost cells are defined on each side of the interface [71] [72] and appropriate schemes are applied to the jump of each quantity. As defined above, the interface is characterized through the distance function, and jump conditions are extrapolated on some nodes on each side of the interface. Following the jump conditions, the discontinued functions are extended continuously and then derivatives are estimated. Heaviside functions are designed according to the distance function in order to provide a characteristic function for the two-phase medium. They follow the functions proposed by [73] according to formula (6) in its publication. Concerning discrete Dirac functions, they are built in a similar way and regularized by a properly set cosine function. These techniques have been presented and validated in previous works, *e.g.* [36].

### 3.5 The DyJeAT code

DyJeAT (Dynamics of Jet ATomization) is an in-house computational fluid dynamics library developed at ONERA. Velocity/pressure coupling is ensured with classical projection methods [74] [75]. In the same way as the ARCHER code, the Ghost Fluid method [76] is used to deal with surface tension forces as well as density and viscosity jumps. The Level-Set (LS) approach is also used for tracking interfaces and LS-VOF coupling is also used to improve mass conservation. An adaptive mesh refinement (AMR) capability has been added to DyJeAT in order to concentrate computational effort where it is most needed. It is based on block-structured AMR. Details of implementation and verification can be found in [77]. As the physics of atomization processes involve many spatial scales, generating a wide range of droplet sizes with large density and viscosity ratios, each scale has to be resolved with an appropriate method to ensure the conservation of mass and momentum and satisfy the jump conditions across the interface. To address these problems, the LS-VOF approach is coupled to a particle tracking technique (*via* an improved Eulerian-Lagrangian coupling) to capture the droplet dynamics [78].

### 3.6 Pros and cons of different codes

Code	Interface tracking	Navier-Stokes velocity-pressure coupling	Capillary forces	Grids	Solvers
Archer	CLSVOF	Projection method	Ghost fluid	Cartesian staggered	BiCGStab Multigrid
DyJeat	Level set	Projection method	Ghost fluid	Cartesian staggered	BiCGStab Multigrid
Gerris	Geometrical VOF	Projection method	CSF with height functions	Collocated and AMR	BiCGStab Multigrid
Jadim	Implicit VOF	Projection method	CSF	Cartesian staggered	BiCGStab Multigrid
Thetis	Geometrical VOF	Augmented Lagrangian	CSF with smooth VOF	Cartesian Staggered	BiCGStab ILU

Table 4: Summary of the numerical methods used in the various codes.

All the codes used in the present work are based on finite volumes but with different variants of the methods. Obviously, each code can lead to a different result for a given grid, due to variations in the methods used. Table 4 is given to clarify the comparisons of the model and numerical method used. Schematically, the codes cover the broad range of numerical methods that can be found in literature for simulating multiphase flows using the sharp interface approximation described above. This approach is sometimes called direct or detailed to contrast it with other approaches that depart from the sharp interface approximation. Four of the codes use staggered grids while one (Gerris) is using a collocated grid. Staggered grids have several advantages: a more accurate pressure solution, and the avoidance of spurious “red-black” velocity oscillations. However Gerris has demonstrated high accuracy on test cases [5, 65] and ten years of experience with Gerris show almost no occurrence of spurious oscillations. Four codes are using projection velocity-pressure coupling that contains a time splitting error while one code (Thetis) uses an exact augmented Lagrangian approach. This technique is exact if the residual of the iterative solver is zero at machine accuracy. In terms of interface tracking, Gerris and Thetis are using a geometrical VOF-PLIC technique while Jadim utilizes a FCT scheme to directly approximate the hyperbolic advection equation on the VOF. DyJeat uses the Level Set method whereas Archer couples this method with VOF-PLIC in order to improve mass conservation of Level Set and also better inertia treatment in the momentum conservation equation. Concerning surface tension, the most accurate approaches are the Ghost fluid that uses jump relations at the interface and the CSF with height functions [5]. Thetis and Jadim uses less sophisticated capillary force approximations that are known to generate more spurious currents than other methods. To finish with numerical methods, all projection techniques are solved with iterative BiCGStab II solver preconditionned with a multigrid algorithm while Thetis and the coupled augmented Lagrangian method uses BiCGStab II and an incomplete LU preconditionner, because the linear system is not symmetric and more difficult to solve than with the projection. The major drawback of the Thetis solver is that its parallelization is keeping a good speed-up until 1000 processors but it can hardly handle in the present form more processors due to the ILU preconditionner. On the contrary, the multigrid preconditionner used in projection is nicely extendable in parallel until 100000 processors.

## 4 Benchmark of phase inversion

The teams that have participated to the present benchmark have each run their own code. All the codes were run on  $256^3$  grids. Moreover one of the codes (DyJeAT) was run on a sequence of much finer grids in order to provide a test of convergence. Cross-comparisons lead us to conclusions on the physical behavior of the numerical methods and also on the physical meaning of the simulations.

### 4.1 Case 1: a phase inversion problem with few fragmentation events

Parameter	Value	Units
$t^* = t/t_c$	$\frac{t}{t_c}$	-
$E_{p,1}^f$ the potential energy in fluid 1 for $t \rightarrow \infty$	0.643	J
$E_{p,2}^f$ the potential energy in fluid 2 for $t \rightarrow \infty$	0.1035	J
$E_{k,1}^* = \frac{E_{k,1}}{(1/16)\rho_1 U_g^2 H^3}$	$\frac{E_{k,1}}{E_{k,1}}$	-
$E_{k,2}^* = \frac{E_{k,2}}{(1/16)\rho_2 U_g^2 H^3}$	$\frac{E_{k,2}}{E_{k,2}}$	-
$H^3/8$ the final volume of fluid 1 in the top part of the box	0.000341	$m^3$
Maximum of enstrophy in fluid 1 (DyJeAT on a $512^3$ grid)	0.000125	$m^3.s^{-2}$
Maximum of enstrophy in fluid 2 (DyJeAT on a $512^3$ grid)	0.0733	$m^3.s^{-2}$
$3H^2/4$ the initial interfacial area of the drop of fluid 1	1.3759	$m^2$
	0.0075	

Table 5: Parameters used to define the dimensionless variables in case 1.

In this section we present the numerical results pertaining to case 1. The characteristics of this case are summarized in Tables 1-3. The macroscopic quantities defined in section 2.3 were computed by the five codes described in the previous section. Dimensionless data are considered according to the definitions indicated in Table 5.

The potential and kinetic energies are mostly dependent on the large scales of the flow and can thus be dubbed “macroscopic” quantities. A convergence study for these quantities was carried out on  $128^3$ ,  $256^3$  and  $512^3$  grids with the DyJeAT code. The corresponding results are reported in Figure 3. There is still some difference between the  $256^3$  grid and the  $512^3$  grid for fluid 2 around time 2.5, although not in fluid 1. For the sake of simplicity in what

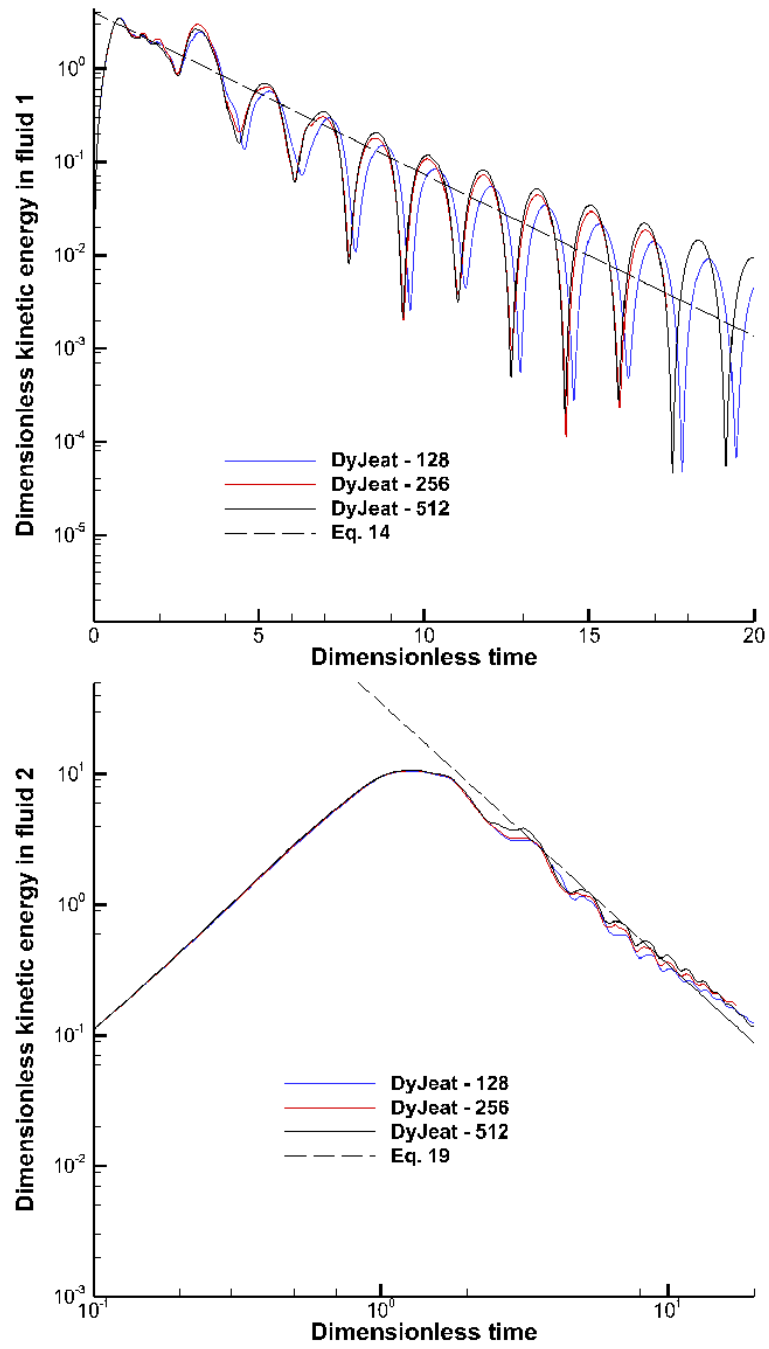


Figure 3: Grid convergence of kinetic energies for case 1 with DyJeAT.

follows we will consider it to be the reference solution, although this may

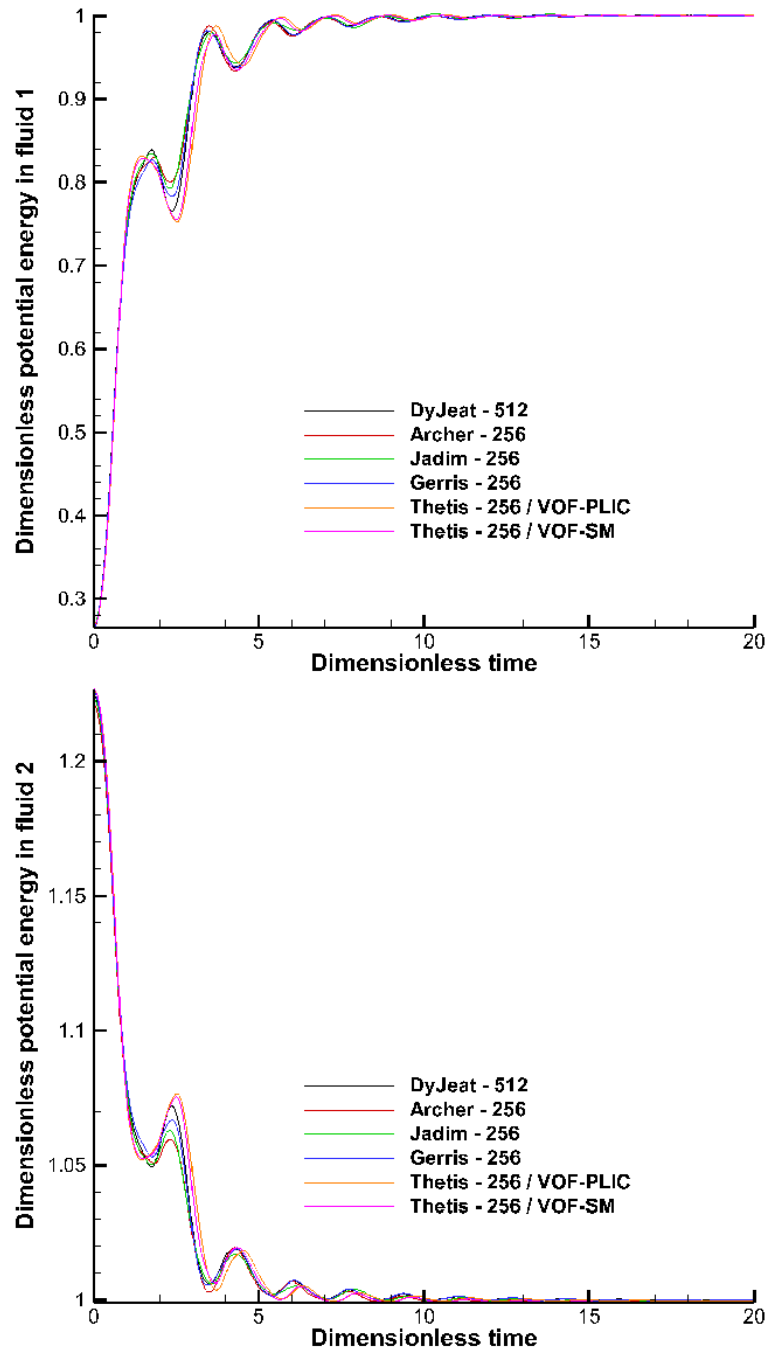


Figure 4: Potential energies for case 1.

not be a fully converged solution after time 2.5 . We note that since as

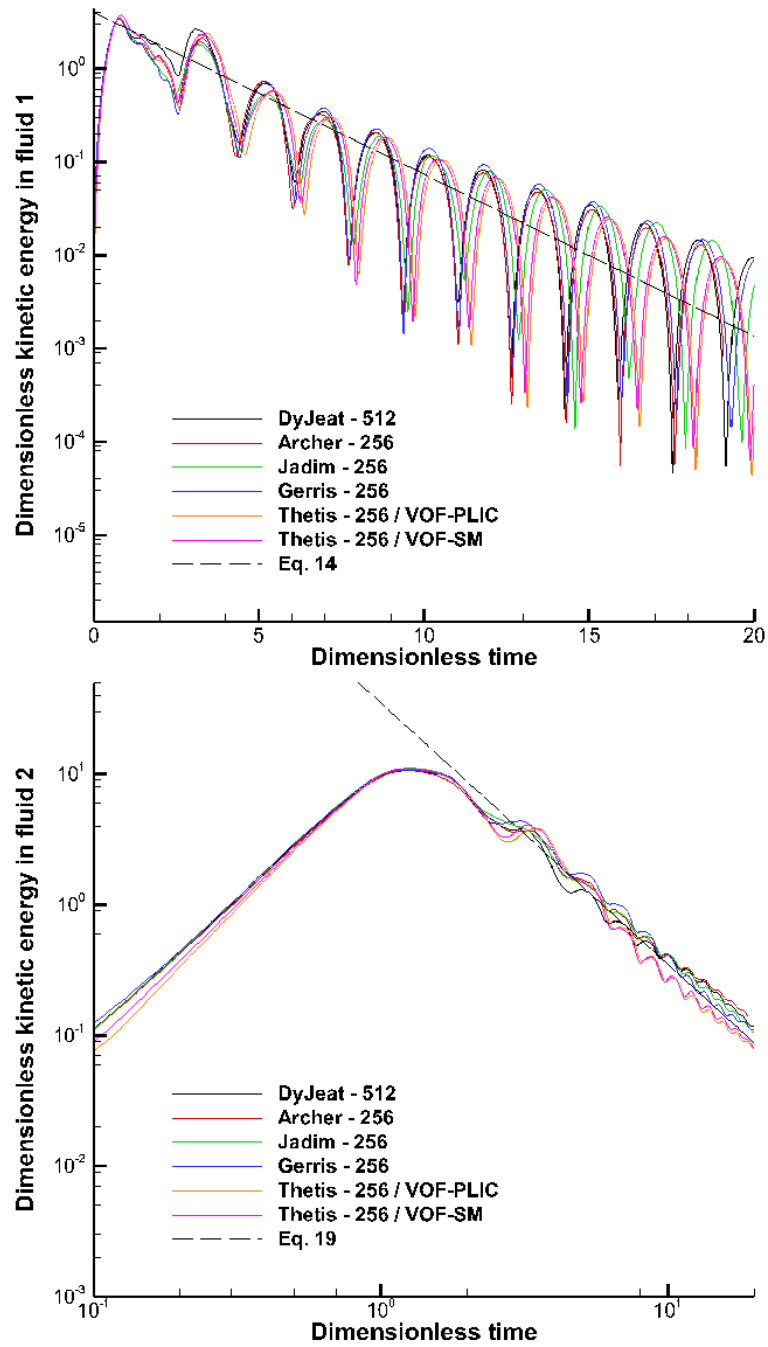


Figure 5: Kinetic energies for case 1 in log-linear (top) and log-log (bottom) coordinates.

shown in Table 5 the kinetic energy is scaled by  $(1/16)\rho_n U_g^2 H^3$  for fluid  $n$ , the maximum kinetic of fluid 2 in the scaled variables is  $8(u_K/u_G)^2(\rho_1/\rho_2) = 11.1375$ . This is close to the maximum of the fluid 2 curve on Figure 3. The fact that the kinetic energy is close to its upper bound also means that  $U_K$  is close to the  $L_2$  norm of the velocity, and that our Reynolds and Weber number estimates are accurate with the  $L_2$  norm velocity.

The evolution of the potential and kinetic energies of the other codes is plotted in Figure 4 and Figure 5, respectively, together with the reference solution. Computations were run on a  $256^3$  grid. The results provided by all five codes on various grids are in approximate agreement with each other and with the reference solution for these quantities. Around time  $t^* = 3$  we see differences between all the codes during the first oscillation arc of the potential energy. At later times, the oscillations of all the codes are superposed, except for the two Thetis codes, and to a lesser degree the Jadim code. For the kinetic energy the behavior is more complex as we see differences between the behavior in fluid 1 and 2. However for both fluids, at large times the kinetic energy predicted by the Archer code is the closest to the reference solution. This may be due to the non-converged character of the DyJeAT reference solution for  $t^* > 2.5$ , which would make agreement with Archer easier since both codes are at least partially Level-Set based. In other words, Archer being the code most similar to DyJeAT will be the most likely to agree with the reference. Figure 4 indicates that phase separation is achieved after a dimensionless time equal to 15. The dimensionless frequency  $f$  of the waves observed at the surface of the light fluid is about 0.6.

According to Figure 5, the kinetic energy decreases as  $e^{-\alpha t^*}$  in fluid 1, which is referred to as Stokes' decay law (18), whereas it decays as  $t^{*-2}$  in fluid 2, which we refer to as the turbulent decay law (23). The origin of these decay laws and the physical assumptions on which they are based are discussed in Appendix A.

To characterize the phase separation on a macroscopic point of view, the volume ratio of fluid 1 occupying the top  $H/8$  part of the box is plotted in Figure 6. A convergence study was carried out on  $128^3$ ,  $256^3$  and  $512^3$  grids with the DyJeAT code. This time the difference between the  $256^3$  grid and the  $512^3$  grid is much smaller than the difference between the  $256^3$  grid and the  $128^3$  grid. Again, it is observed here that all codes predict evolutions close to each other and to the reference solution. The code-to-code comparison indicates some phase shifts and various damping rates at large times. The largest difference is found for the Thetis code, followed by the Jadim code. The Archer code is even closer to the reference and the

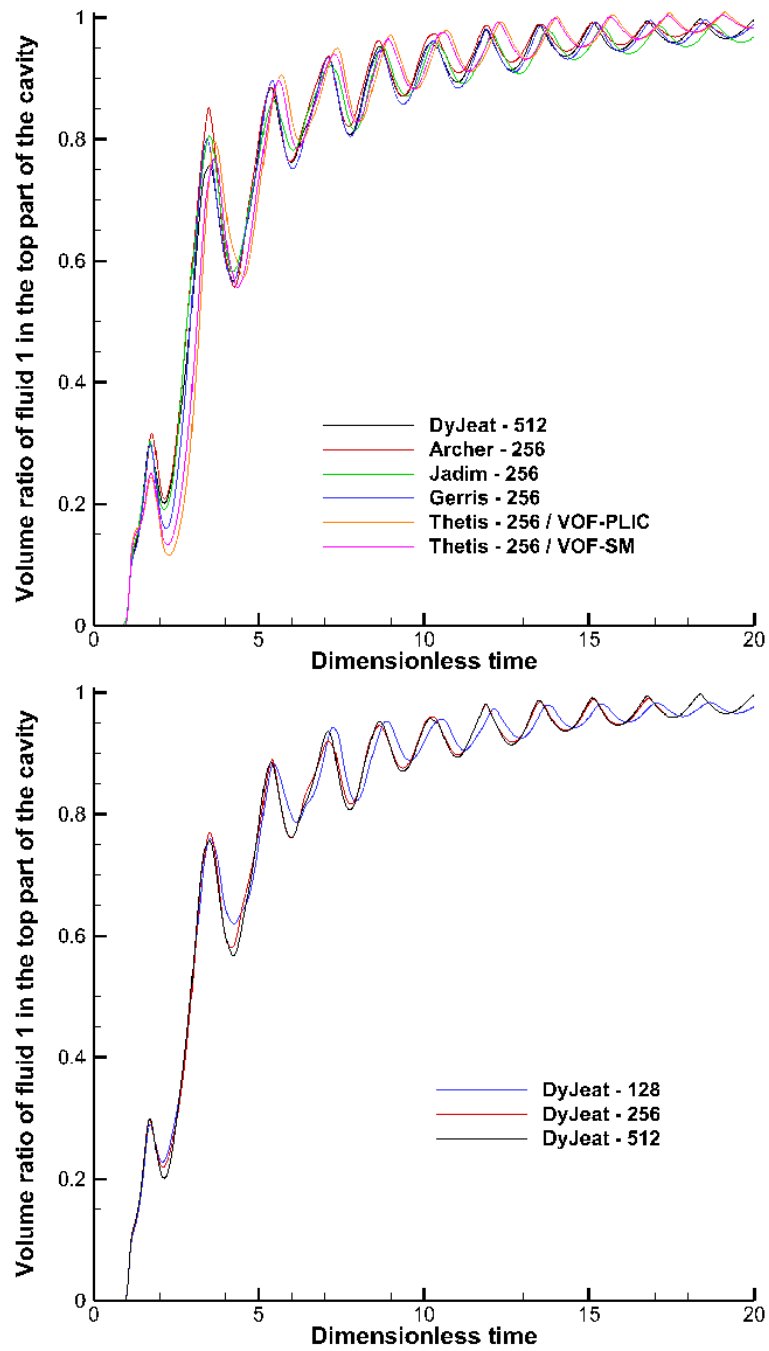


Figure 6: Evolution of the volume ratio of fluid 1 in the top part of the box in case 1.

Gerris code is closest. One possible explanation could be the quality of mass conservation in the codes, since it would directly influence the amount of fluid in the top part. Another explanation would be the accuracy of energy conservation since it drives the oscillations seen. A third explanation for the different behavior of the codes is their more or less diffusive character. Level sets have the smoother indicator function while VOF have the sharper, and Jadim has an intermediate behavior. Clearly the ranking of the codes cannot be exclusively alloted to the conservation of mass since all the VOF codes are supposed to do well in this respect but do not perform equally well in the comparison. In addition, the effective initial volume of light fluid is not initially strictly equal to the theoretical volume of  $H^3/8$ . Also in some cases one observes liquid drops trapped on the domain walls. Both of these effects explain the fact that numerically obtained volume ratios tend to a value slightly less than 1.

These plots suggest that phase separation is almost completed after more than 20 time units, which is slightly longer than what was observed by examining the potential energy.

Figures 7 and 8 display the instantaneous values of the enstrophy in both fluids. Although all codes were shown to agree well on other macroscopic quantities, the magnitude of the enstrophy peak differs dramatically for each of them. The location of this peak is found to occur at  $t^* \approx 2$  (resp. 3) for all codes in fluid 1 (resp. fluid 2). However, differences in magnitude up to 80% are observed, depending on the grid and the code. The spatial convergence study of enstrophy carried out with DyJeAT is illustrated in Figure 9. Although the enstrophy seems to converge in fluid 1, its peak increases with the grid resolution in fluid 2 and no convergence is reached even on the  $512^3$  grid. Therefore, although primary moments such as potential and kinetic energies or volume ratio of the light fluid suggest that a real DNS was achieved, the analysis of higher-order moments such as enstrophy invalidates this hope. Despite the large discrepancies noticed between all codes, it is interesting to observe that they all provide a  $t^{*-3}$  temporal decay law which may be shown to correspond to a turbulent scaling (see Appendix A).

The interface shape and isovalues of vorticity magnitude at  $t^* = 3$  (which corresponds to the peak within fluid 2 in Figures 7 and 8) are reported in Fig. 10. The maximum magnitude of the vorticity is found to be concentrated in the near-wall regions and in regions where the large blob of light fluid that has risen during the phase separation process undergoes high deformations. Finer vortical structures are clearly captured by the finer grid inside fluid 2

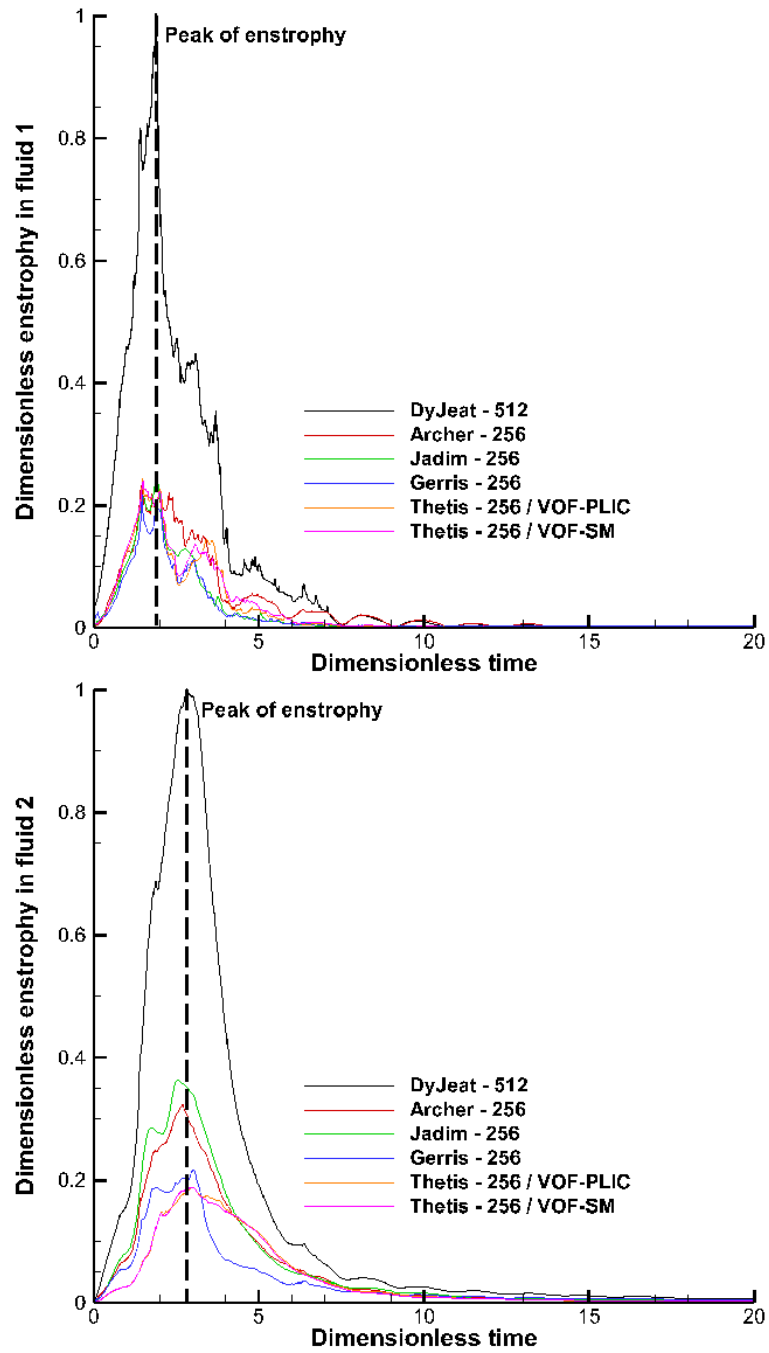


Figure 7: Enstrophy for case 1.

(near the bottom corners for instance). When the large blob of light fluid

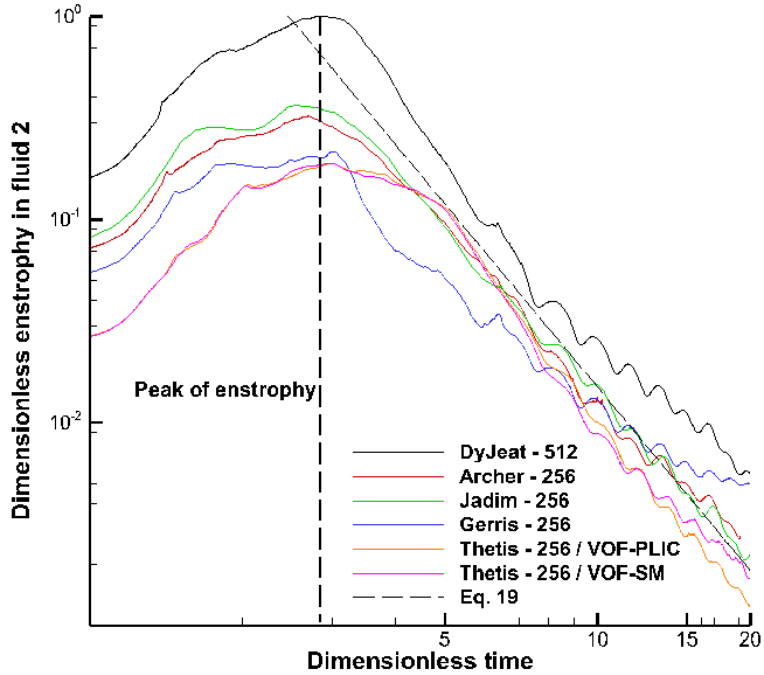


Figure 8: Enstrophy for case 1 in log-log coordinates.

moves from one side of the box to the other, heavy fluid is trapped between some of them and the wall, generating high shear (hence high vorticity) regions. Such boundary layers are clearly not fully resolved with the grids used in the present work, which explains the lack of convergence observed for the volume-averaged enstrophy.

In single-phase turbulent flows, Direct Numerical Simulation is known to require a number of grid points of the order of  $Re^{9/4}$  [79] [80]. Provided no scale smaller than the Kolmogorov microscale exists in the phase inversion problem investigated here, and considering the integral scale Reynolds number based on the parameters introduced in section 2.3, at least  $13700^{9/4} = 2.03 \cdot 10^9$  grid points would be necessary to achieve a real DNS for case 1. However the finest grid used to simulate case 1 had only  $512^3 = 1.35 \cdot 10^8$  grid points. This is an indication that the maximum grid resolution used in this work is not sufficient. In addition, as we are considering two-phase flows with severe jumps in the physical properties, especially viscosity, properly capturing the interfacial vortical layers requires that a sufficient number of grid points be located around the interfaces. The 2D slice shown in Figure 10 clearly indicates that the vorticity magnitude reaches its maximum near the interfaces, a region where high shear rates take place, owing to the large vis-

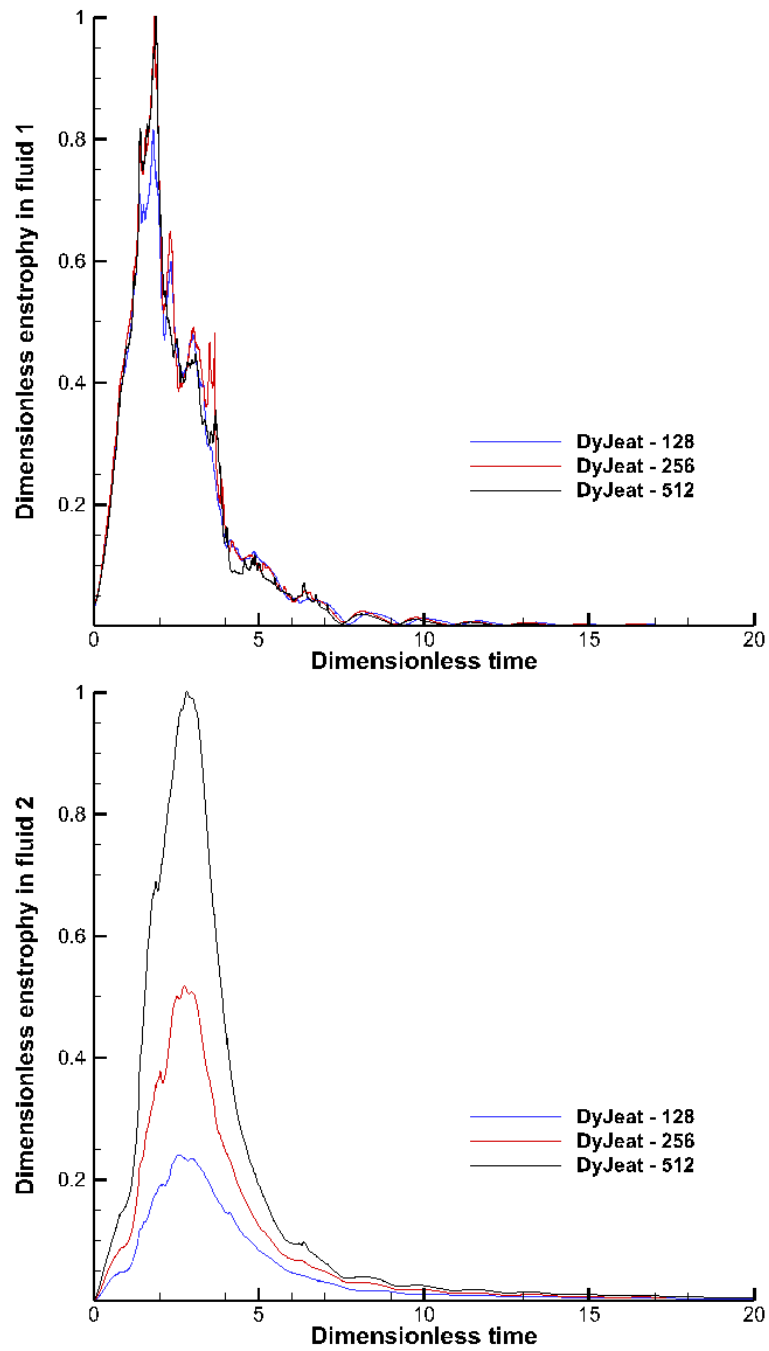


Figure 9: Convergence of enstrophy for case 1.

cosity contrast. Therefore we may suspect that the way the local viscosity is

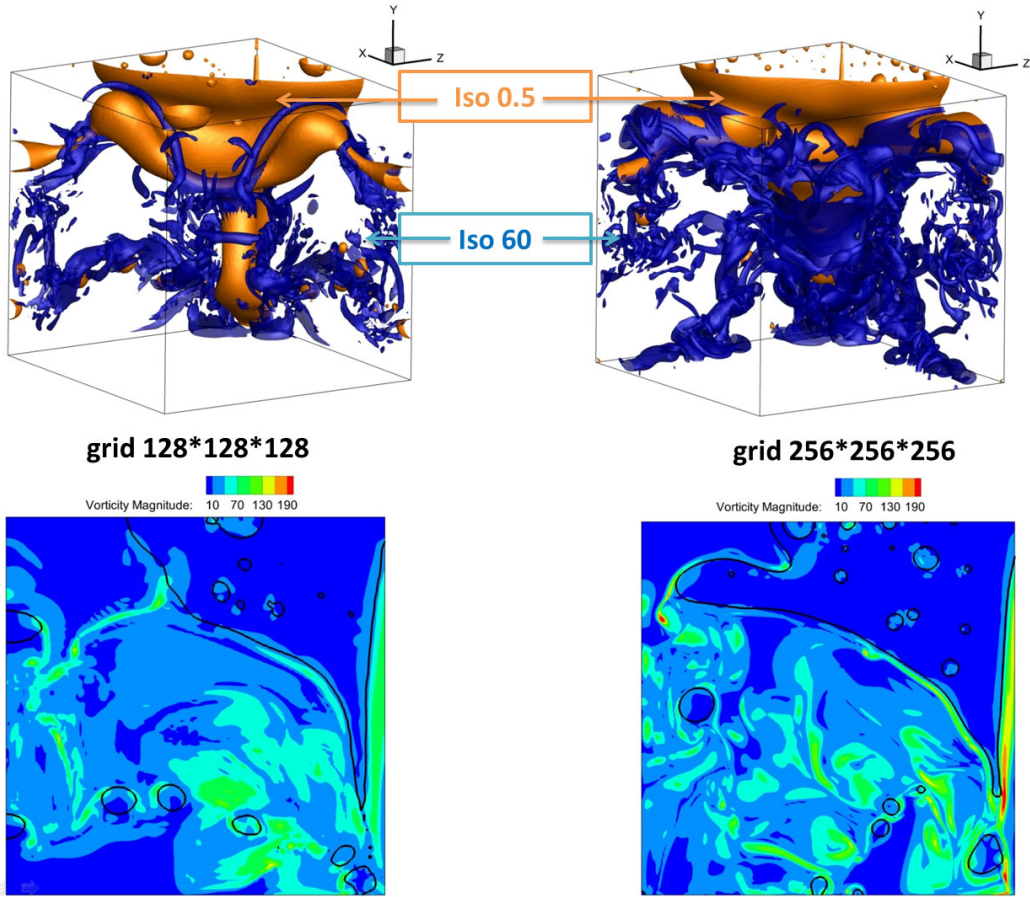


Figure 10: Vorticity structures and interface shape for case 1 - top: iso-60 vorticity magnitude (blue) and iso  $C = 0.5$  interface (orange surface) - bottom: isoline of vorticity magnitude and interface shape (black line) obtained with Thétis on two different grids.

estimated as a function of the local volume fraction plays a role in the local vorticity magnitude. Indeed, an arithmetic average is generally performed but there are good reasons to rather favor an harmonic average [81–83]. To avoid this possible influence, we re-computed case 1 with the DyJeAT code while considering the same viscosity in both fluids. The corresponding results are discussed in Appendix B. They show that grid convergence of enstrophy is still not achieved when the viscosity is set to  $0.1 Pa.s$  (the corresponding Reynolds number is 130) although the enstrophy excursions are less violent. A similar study was performed by some of us [84] with the conclusion that sheet breakup may be responsible for spurious large enstrophy even at re-

duced Re and La. The obvious conclusion of these additional computations is that the differences found among the enstrophy evolutions are not due to effects of an imprecise numerical modeling of the viscosity jump but to other effects requiring further study. We also note that in the atomization simulations of some of us [12] enstrophy as measured statistically is not diverging upon grid refinement. Hence the results produced by the five codes do not correspond to a Direct Numerical Simulation: convergence is achieved on quantities dominated by the large-scale motions, such as the kinetic and potential energies, but it is not on enstrophy for which the main contribution is from the small-scales.

## 4.2 Case 2: a phase inversion problem involving many break-up events

Fluid	Maximum Enstrophy
1	$103 \text{ m}^3 \cdot \text{s}^{-2}$
2	$1049 \text{ m}^3 \cdot \text{s}^{-2}$

Table 6: Values of enstrophy used to make the plots nondimensional in case 2 compared to 5, obtained from DyJeAT on a  $2048^3$  grid.

In this section, we comment on the simulations of case 2 whose specific characteristics are provided in Table 2. The corresponding dimensionless data are given in Table 3. The characteristic time is now  $t_{c,2} = H_2/(2U_{g,2}) = 2.032$  and the dimensionless time is now  $t^* = t/t_{c,2}$ .

Again, in order to examine grid convergence, the numerical simulations were run on five grids *i.e.*  $128^3$ ,  $256^3$ ,  $512^3$ ,  $1024^3$  and  $2048^3$  for DyJeAT. (It has to be noted that 30 million hours of CPU time have been necessary during two years to perform the simulation on the finest  $2048^3$  grid.) This study is displayed on Figure 11. The data of the three finest grids superpose until approximately  $t^* = 4.5$ . After that time, the comparison of the three finest grids shows that there is no longer a well-characterized convergence: the predicted kinetic energy varies irregularly with the grid size, with the difference between the  $2048^3$  and the  $1024^3$  often larger than the difference between the  $1024^3$  and the  $512^3$  grid. This behavior starts at  $t^* = 1.75$  and becomes marked after  $t^* = 5$ . This can only indicate one thing: despite the kinetic energy being mostly in the large scales, the small scales influence strongly the evolution of the kinetic energy. These small scales may for

example be related to coalescence events involving the perforation of thin liquid sheets, which will have a strong influence on the large scales.

Because of the observed convergence behavior of DyJeAT, its  $2048^3$  kinetic energy can be taken as a reference, with certainty until  $t^* = 1.75$ , and roughly speaking until  $t^* = 5$ . The other numerical simulations were run on a  $256^3$  grid for Archer, Jadim, Gerris and Thétis. Similar to the observations in case 1, the results provided by the five codes are in approximate agreement as far as the time evolution of the potential and kinetic energies is concerned, even if larger discrepancies are observed compared to case 1. These evolutions are displayed in Figures 12 and 13. The behaviors of the codes are diverse. For example, the Gerris code performs well for the kinetic energy of fluid 2. However for the kinetic energy of fluid 1 the Gerris code predicts a significantly different oscillatory dynamics as soon as  $t^* = 1.5$ . In fact, for fluid 1, all codes are close to the reference, except Gerris, until time  $t^* = 2.5$  and then all codes diverge from the reference. For fluid 2 Gerris and Thetis behave better than the other codes at times  $2 < t^* < 3$ . We have no explanation for this behavior.

An oscillating behavior is still present, even though it is less regular than in case 1. In all simulations, the kinetic energy decays as  $t^{*-2}$  in fluid 2, as already found with case 1. In fluid 1, the exponential Stokes decay law is clearly more difficult to obtain as large amplitude variations are observed. Compared to case 1, the turbulent intensity in fluid 2 is larger, especially in the bottom part of the box, and thus provides a strong forcing to the large blob of light fluid that stands on top of it. This is why the oscillatory motion of fluid 1 is more complex than in case 1 and its decay does not strictly follow the purely viscous Stokes law.

The time histories of enstrophy are plotted in Figures 14, 15 and 16. Again, all codes find the peak value nearly at the same time, namely  $t \approx 2.5$  in fluid 1 and  $t^* \approx 4$  in fluid 2, although the code-to-code differences are significantly larger than in case 1. The delay in the development of enstrophy in fluid 2 (compared to fluid 1) was not observed in case 1. It is a direct consequence of the higher Reynolds number: vortical layers develop quite quickly in the more viscous fluid 1, but a significantly longer time is required for shear regions to develop in fluid 2, owing to the prevalence of inertial effects. Again, the enstrophy magnitude increases with the grid resolution and is code-dependent. Compared to case 1, this tendency is reinforced by the large number of break-up events which result in a large population of droplets of fluid 1 that modulates the motion in fluid 2. Whatever the grid resolution, including  $2048^3$ , convergence is not achieved and the finer the

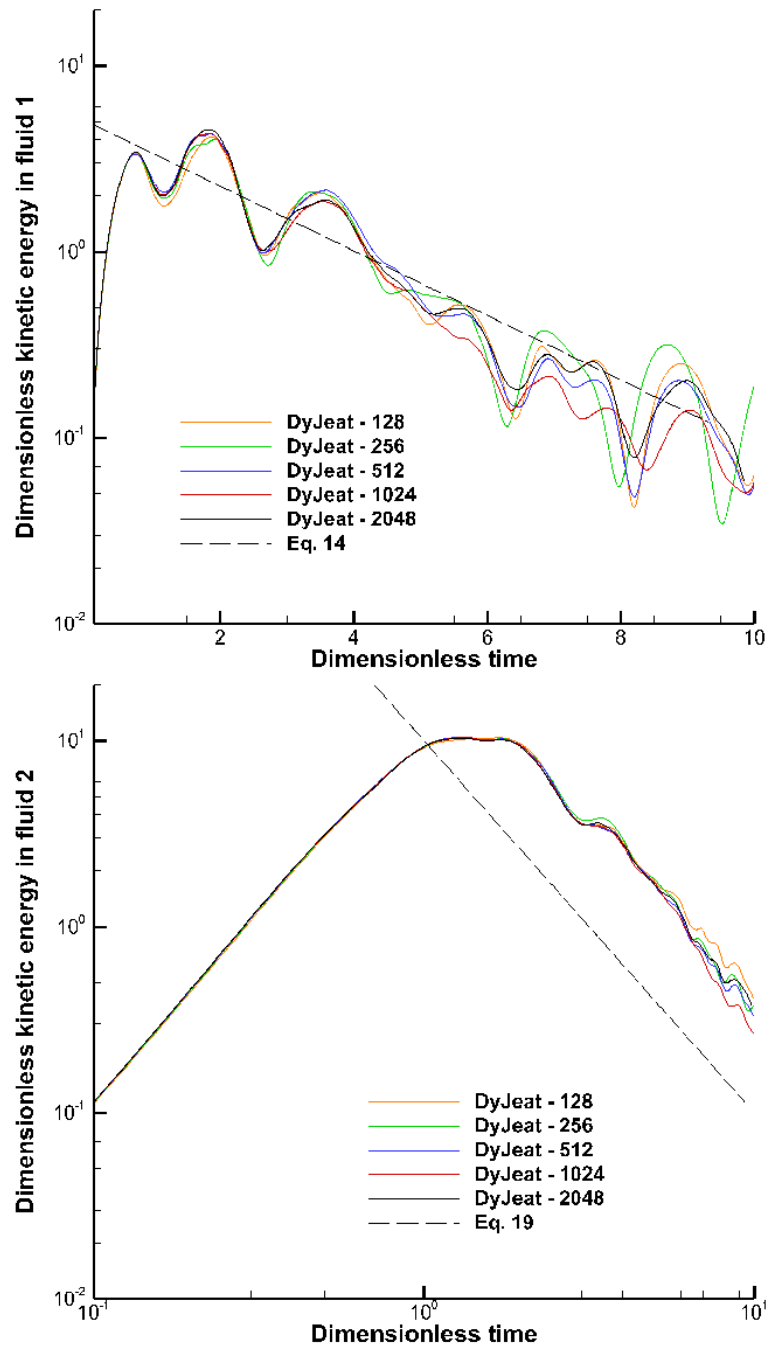


Figure 11: Grid convergence on kinetic energies for case 2 with DyJeAT in log-linear (top) and log-log (bottom) coordinates.

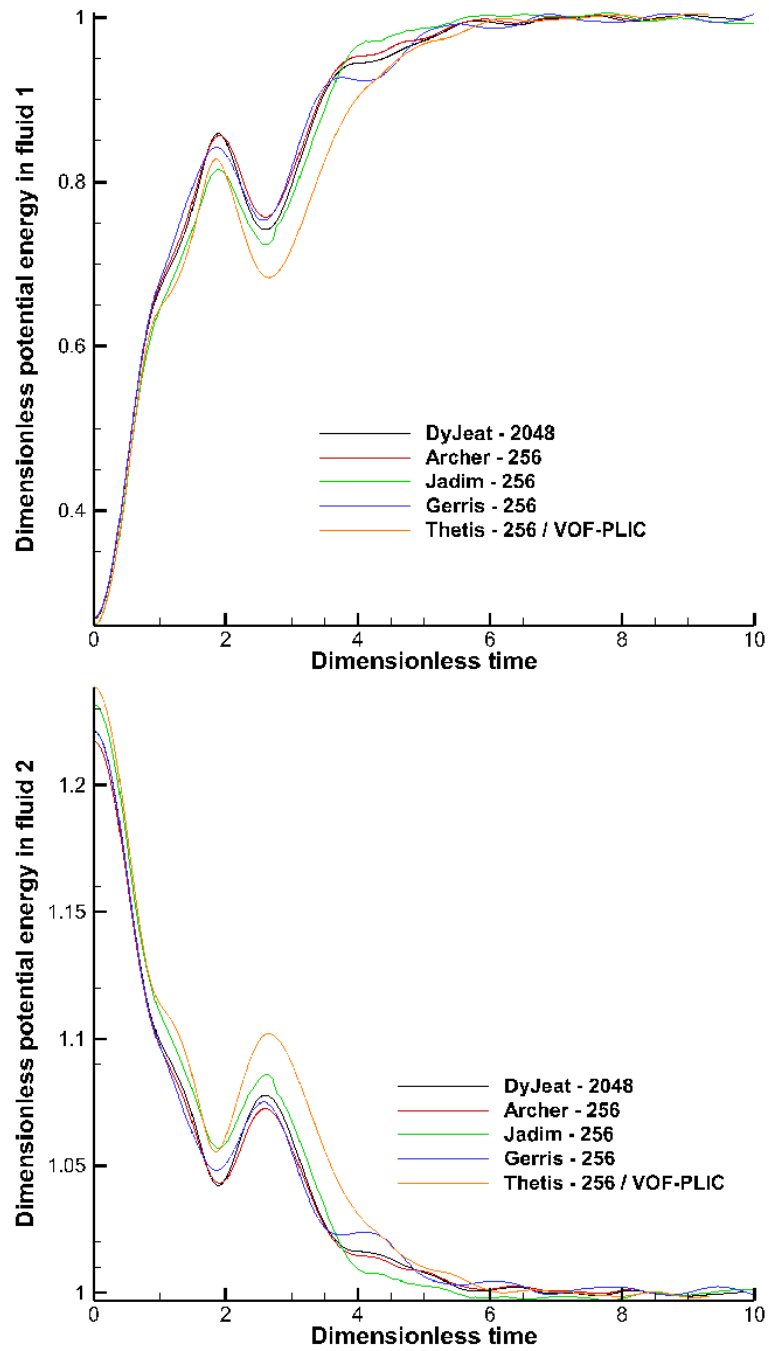


Figure 12: Potential energies for case 2.

grid, the larger the entropy magnitude. As Figure 16 shows, the difference

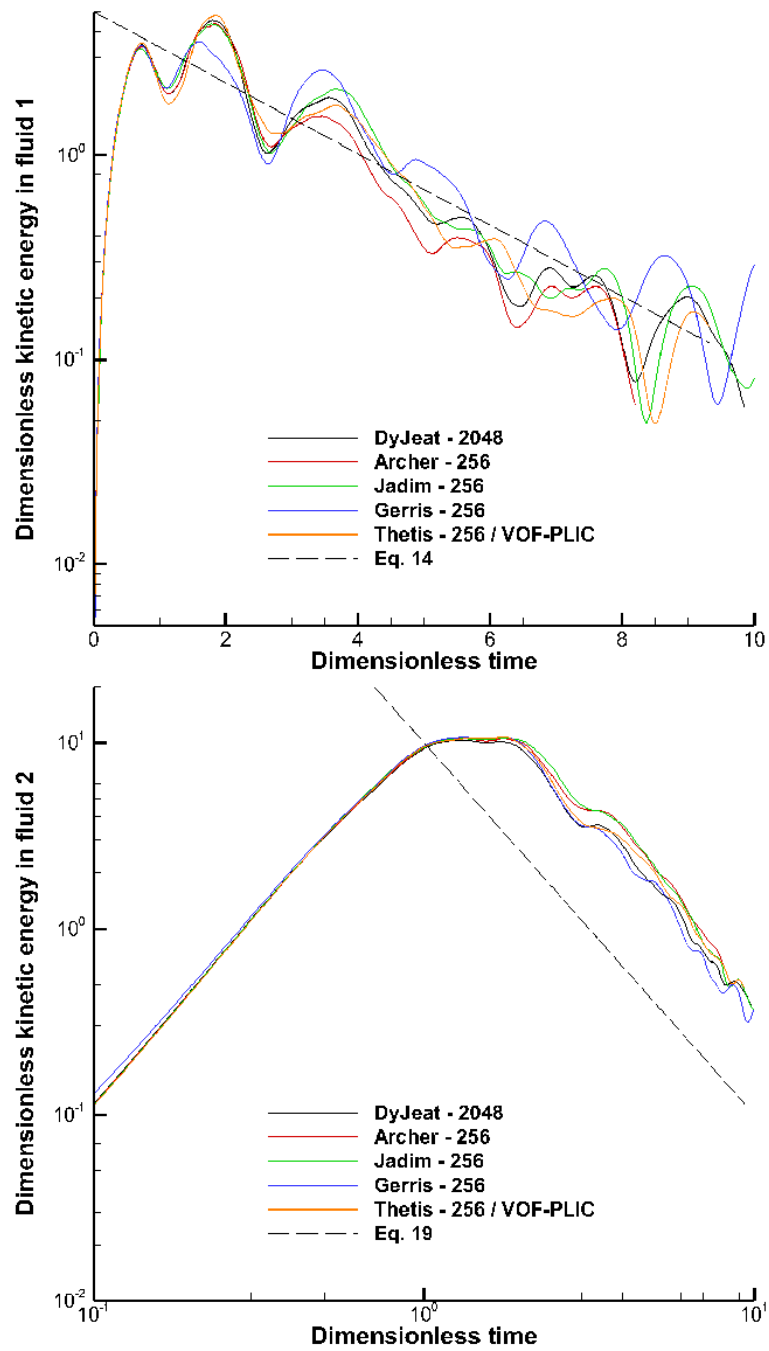


Figure 13: Kinetic energies for case 2 in log-linear (top) and log-log (bottom) coordinates.

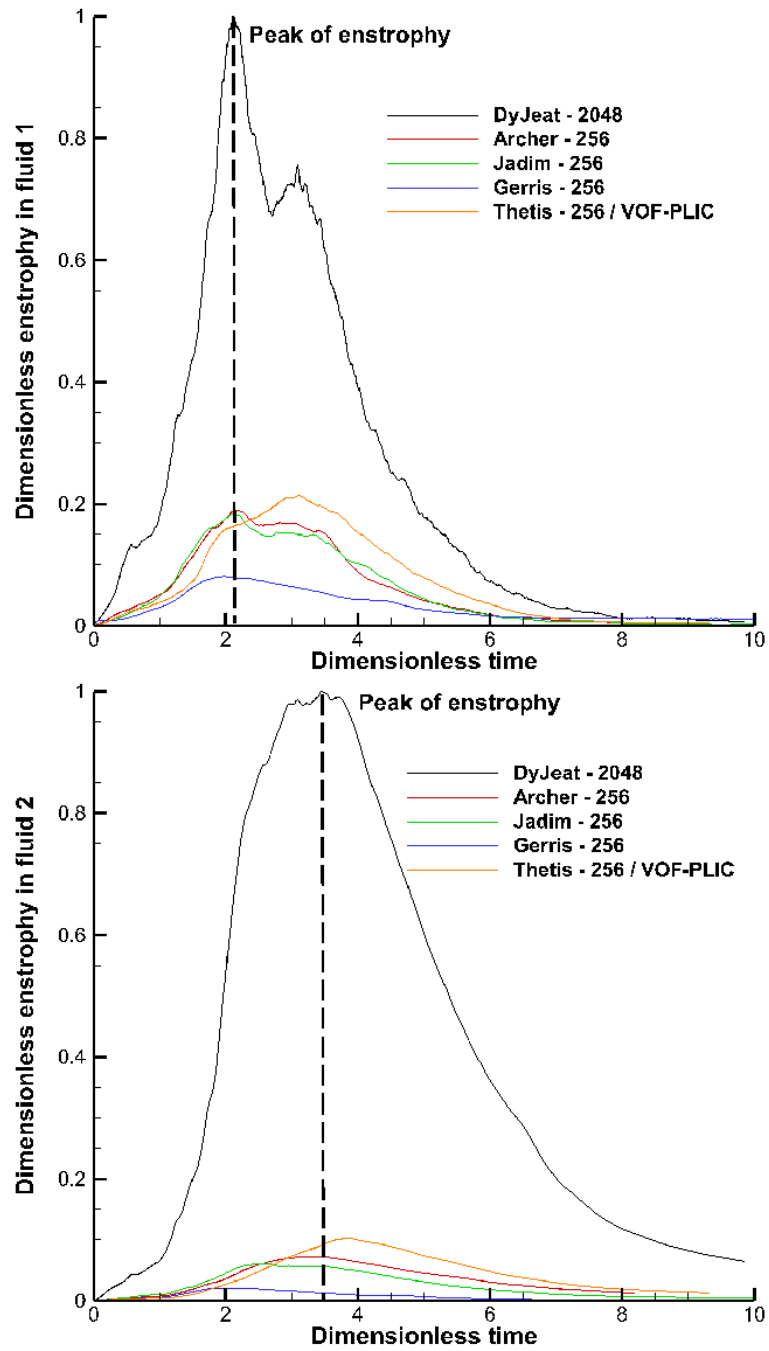


Figure 14: Enstrophy for case 2.

in magnitude between the peak magnitudes obtained with two successive res-

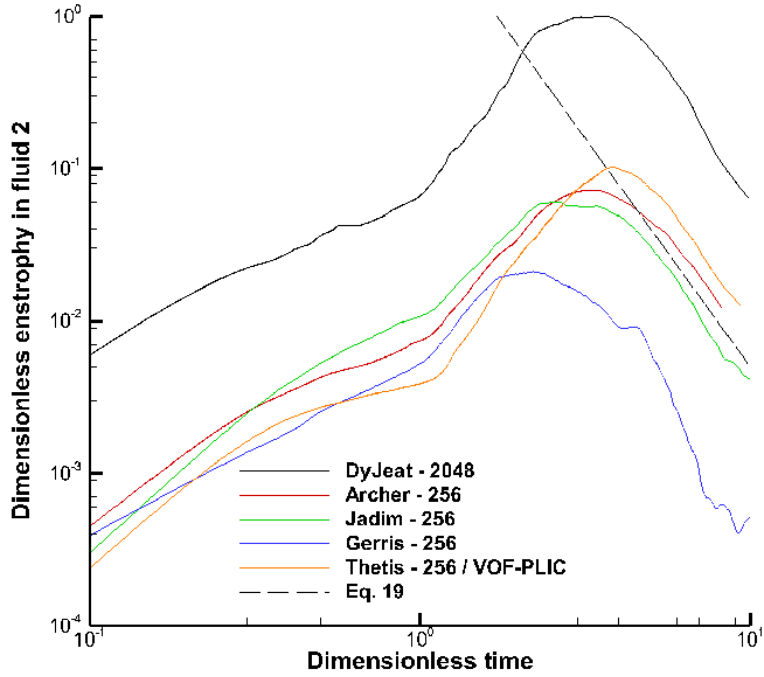


Figure 15: Enstrophy for case 2 in log-log coordinates.

olutions increases as the grid is further refined. This is an indication that the highest resolution considered here is still far from that required to achieve a true DNS. However, in the DyJeAT convergence study, it is observed that the width of the time interval in which the enstrophy differs is decreasing with refinement of the grid, testifying that grid convergence will be reached for a finer mesh. This observation is mainly valid for fluid 1.

A view of the shape of the interfaces at the time the enstrophy is maximum is provided in Figure 19. Large interfacial scales are observed in the top part of the box, with at the same time an important population of small dispersed droplets of fluid 1. Consequently, high-shear regions are more numerous and difficult to capture than in case 1. The vorticity in fluid 2 is modulated by the presence of the light droplets of fluid 1 that first follow the motion of fluid 2 at short times, owing to inertia and viscous effects, and then rise under buoyancy effects. The finer the grid, the smaller the droplets captured by the computation. This feature has a direct influence on the intensity and density of vortical regions in the flow, since the latter are closely related to the phase distribution, *i.e.* to the dispersion of fluid 1 in the present case. Therefore the behavior of the volume-averaged enstrophy depicted above is

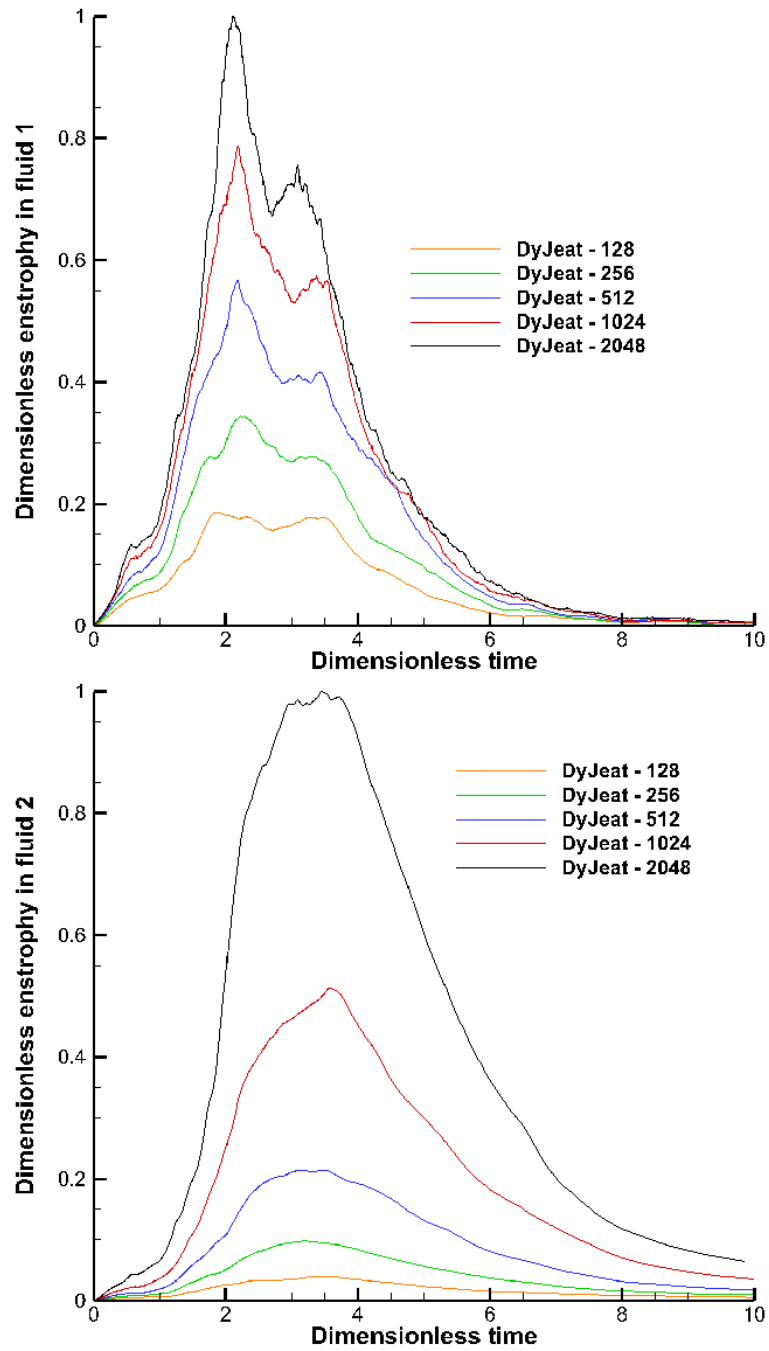


Figure 16: Convergence of enstrophy for case 2.

a direct consequence of this grid-dependent population of droplets.

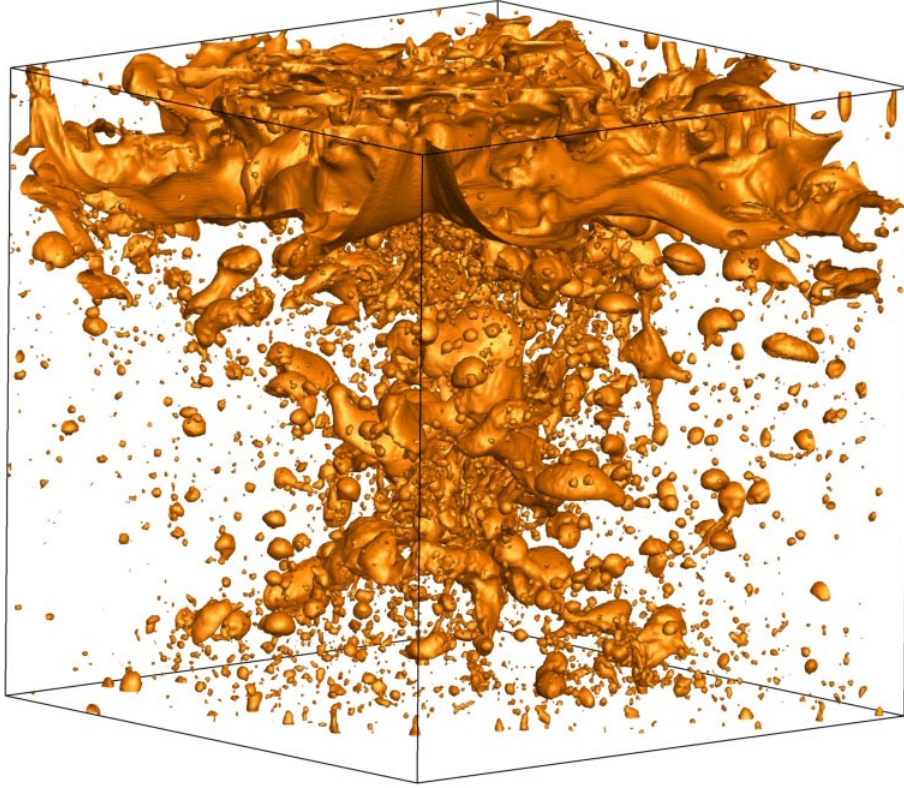


Figure 17: Topology of interfaces for case 2 at  $t^* = 4$  (corresponding to the enstrophy peak) in fluid 2 - Results are from Thétis on a  $256^3$  grid.

In Figure 18 we consider the total interfacial area. For reasons of simplicity, we use the rough approximation for the interfacial area given in equation (7). A convergence study for formula (7) is proposed in Appendix C in the case of a sphere. It is demonstrated that as soon as the grid is refined the error on the interfacial area is going from 50% to less than 20%.

Consider first simulations run on the five grids of DyJeAT. The predicted interfacial area seems to be almost converged on the finest grid. Interestingly the convergence is not monotonic, but the interfacial area first increases for grids  $128^3$  to  $1024^3$  then decreases slightly for the  $2048^3$  grid. This may indicate that there are two types of error involved, one coming from the ability of the scheme to capture correctly all the relevant droplet sizes, and the second from the ability of the code to find, using (7), the area of a droplet that has been correctly formed, at the converged size in DyJeAT. The first effect leads to a larger population of small droplets being produced as the

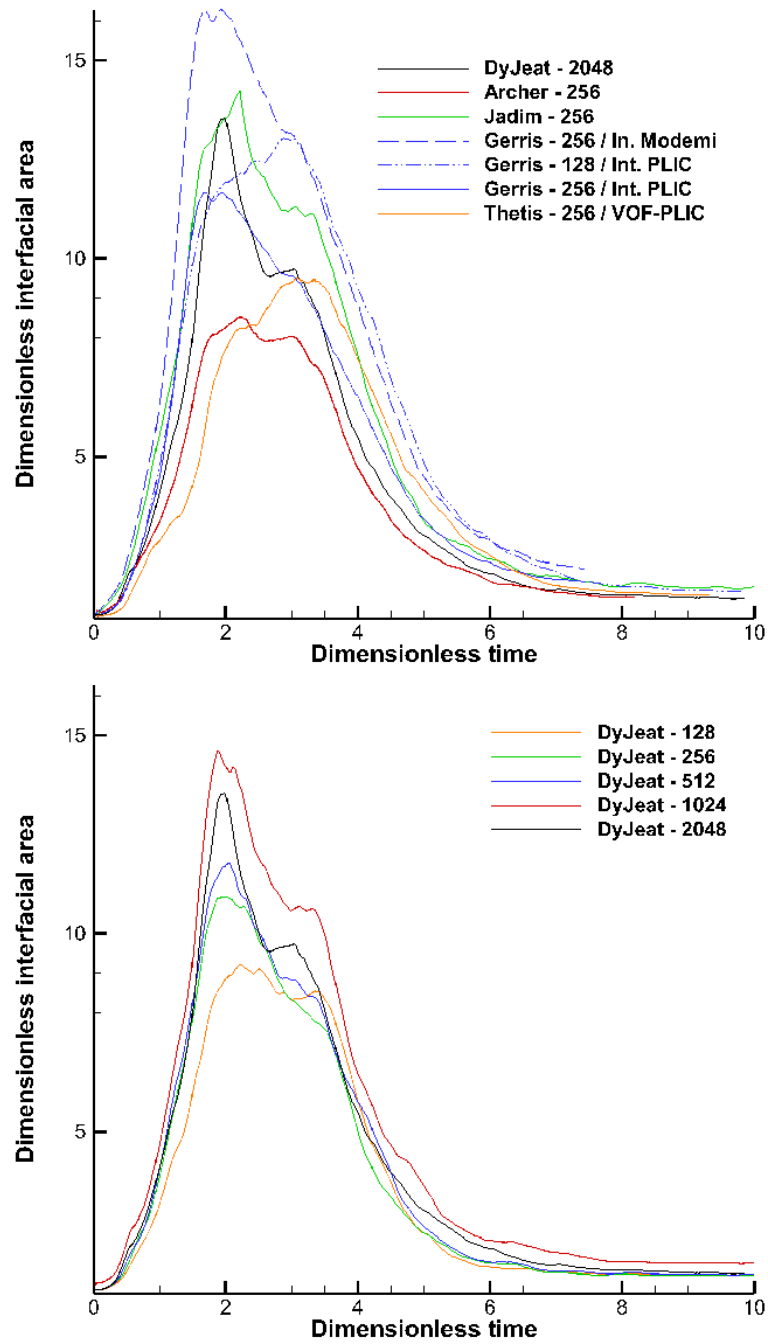


Figure 18: Interfacial area for case 2 using either equation (7) or in the special case of Gerris the PLIC reconstruction. Equation (7) is noted Int. Modemi.

grid is refined from  $128^3$  to  $1024^3$  while the second effect presumably comes from a weaker increase of the number of droplets but a better capture of their area. One can also see that in the Gerris case, where the PLIC surface area is available, the interfacial area is markedly smaller with PLIC than with (7).

The physical mechanism behind the observed interfacial area behavior is easy to comprehend in its broad lines. The initial fast upward motion of fluid 1 atomizes the interface and results in the growth of a population of small droplets, that yields an increase of the interfacial area. However, mysteriously, it can be noticed that the peak value of the interfacial area is not only grid-dependent but also code-dependent. Pure PLIC-VOF codes such as Gerris conserve mass much better and the breakup of thin sheets results in the formation of a large number of droplets, while level-set codes such as DyJeat result in the “evaporation” of small objects. Thus the relatively larger number of droplets at late times in Jadim and Gerris, both VOF codes, and the smaller interfacial area in DyJeAT, a Level-Set code, could be attributed to this fact and not to the use of (7) to compute the interfacial area. However this does not explain why Thetis, also a PLIC-VOF code, has such a small interface area. Other aspects of the codes may explain the properties of droplet atomization and coalescence, such as the implementation of surface tension forces, which varies widely between codes.

This issue needs to be addressed in future investigations because the interfacial area is one of the key parameters in problems involving heat or mass transfer.

## 5 Droplet size distributions

We have performed a study of droplet size distributions using DyJeAT in case 2 at the time of the enstrophy peak ( $t^* = 4$ ). We define the Probability Distribution Function (PDF) as number frequency  $f$  defined as follows. The droplet sizes are measured in the simulations and an equivalent radius  $r$  is obtained for each drop. The equivalent radius may belong in any of a number of adjacent bins  $B_i$  defined as the interval  $B_i = (r_i - \Delta_i/2, r_i + \Delta_i/2)$  where  $r_i$  and  $\Delta_i$  are the bin center and width, and define the bin structure. In our first analysis, the bins are regularly spaced. One defines  $\Delta_i = 1/256$ ,  $r_i = (i - 1/2)/256$  and  $B_i = ((i - 1)/256, i/256)$ . Then the number of droplets whose equivalent radius is in  $B_i$  is noted  $N_i$ .  $N_i$  is approximately proportional to an asymptotic probability  $f$  such that  $f(r_i) = N_i/\Delta_i$  however the approximation does not hold very well for the first bin because  $\Delta_1/r_1$  is

far from small. On Figure 19 we plot  $N_i$  versus  $r_i$ . The observation of these

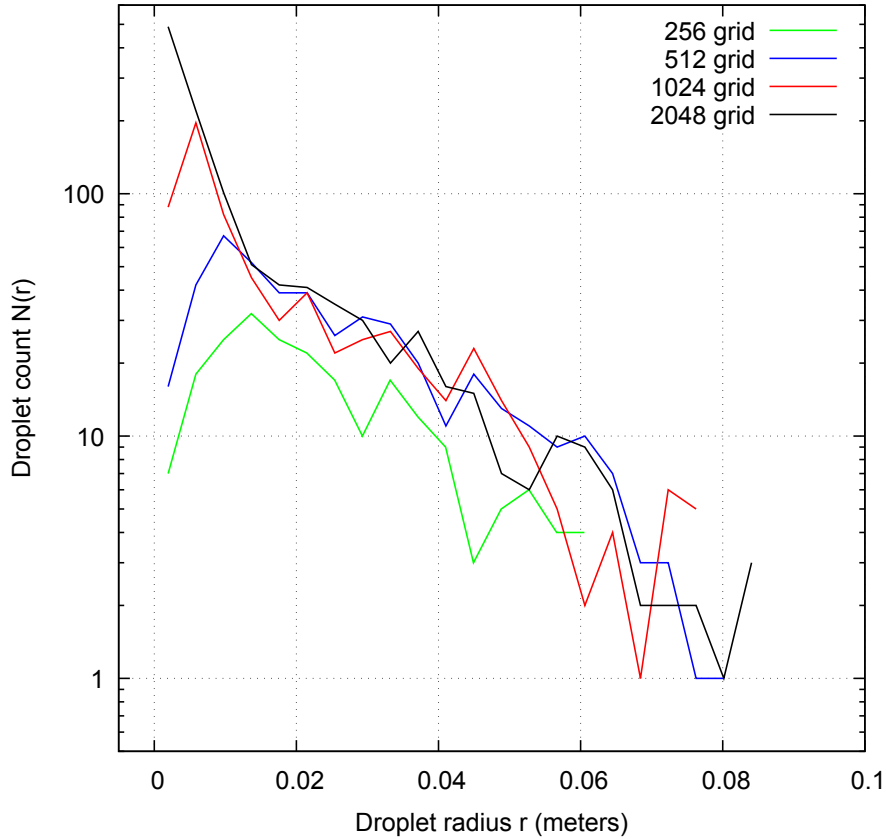


Figure 19: Droplet radius frequency  $N_i$  defined in the text obtained with DyJeAT at  $t^* = 4$ . The droplet radii are in meters and the box size is  $H = 1\text{m}$ .

distributions leads to several remarks. First, the  $256^3$  grid result does not match the others, but instead droplet populations obtained with that grid are systematically less numerous than for the other grids, indicating that the total mass of droplets obtained with that grid is smaller. This can be easily explained by the fact that poorly resolved droplets “evaporate” in a level-set method such as DyJeAT. The uncertainty surrounding the  $256^3$  grid results also leads us not to discuss the results of the other codes for the PDF, which are only available at this resolution. Second, the  $512^3$ ,  $1024^3$  and  $2048^3$  grid results superpose in a region of variable size, going from a minimum radius  $r_m(N)$  to a maximum radius  $r_M(N)$ , with both  $r_m$  and  $r_M$  function of the

grid resolution  $N$ . To be specific, the minimum radius of agreement decreases with increasing  $N$  until approximately  $r_m(2048) \simeq 0.005$  which indicates a range of convergence extending to very small droplet radii for the  $2048^3$  grid. The upper boundary  $r_M(N)$  of the range of convergence is harder to determine, because the large radii are affected by statistical noise. However, it is seen that few additional very large droplets ( $r > 0.07$ ) are seen as the resolution increases from  $256^3$  to  $2048^3$ . Moreover grids  $1024^3$  and  $2048^3$  are in agreement in a wide range with  $r_M(2048) \simeq 0.05$ . Finally we note that the behavior at very small droplet sizes is different for the  $2048^3$  grid and other grids: while the other grids have a cutoff (a fall in droplet counts  $N_1$  and/or  $N_2$ ) at small sizes, the  $2048^3$  grid does not. This is due to the fact that in the  $2048^3$  case the fall in droplet count can only be seen if instead of the peculiar bin  $B_1$  defined above, one subdivides the interval  $(0, 1/256)$  into several smaller bins. We have actually done that and did observe the cutoff even for the  $2048^3$  case.

Indeed, similar effects of the grid refinement, including the cutoff or drop in frequency, have been reported for atomization of liquid jets, especially for level set methods [85] and less markedly for VOF methods [19]. This indicates that  $512^3$  grids are a minimum requirement to have an approximately accurate droplet count at *any* scale, and that  $256^3$  simulations are poorly resolved in the whole range of scales. This explains the poor results on interfacial area with the  $256^3$  simulations of all the other codes. On the other hand, the absence of convergence of the enstrophy does not imply a non convergence of the droplet sizes in the intermediate range  $r_m(N) < r < r_M(N)$ . Another interesting fact is that the large scales are influenced by how the small scales are computed: more large droplets are seen with finer grids, probably because more grid resolution implies less breakup of thin layers or filaments, thus reducing the rate at which large structures break into small ones. In order to better understand the PDF, we plot the computed frequencies for the two most refined grids as a graph of  $\ln(r_i N_i)$  versus  $\ln r_i$  in Figure 20. The first bin  $B_1$  has been excluded due to its particular character, and only the most refined grids  $1024^3$  and  $2048^3$  are shown. Using these coordinates has the advantage that the log-normal PDF appears as a parabola. The log-normal PDF is defined by

$$f(r) = \frac{A}{r} \exp \left[ -\frac{(\ln r - \ln \hat{\mu})^2}{2\hat{\sigma}^2} \right] \quad (12)$$

where  $A$  is normalisation constant,  $\ln \hat{\mu}$  is the logarithmic average and  $\hat{\sigma}$  the logarithmic standard deviation. A parabolic curve corresponding to such a log-normal distribution is shown on Figure 20 to aid the interpretation. This

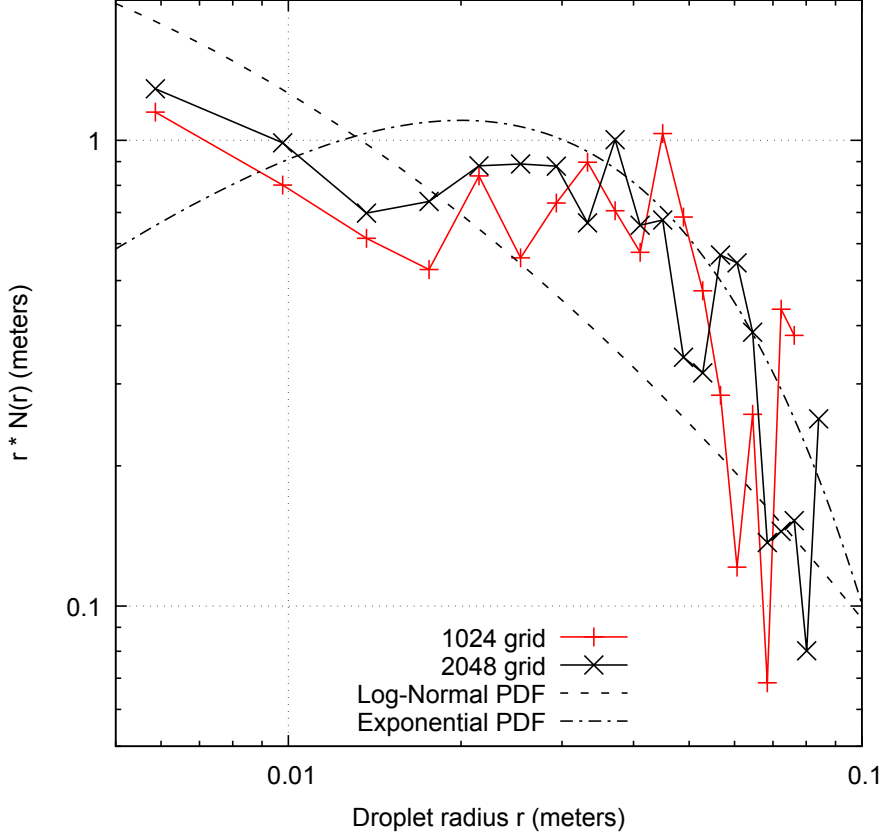


Figure 20: Droplet radius frequencies (probability distribution function) in logarithmic coordinates, with  $r f(r)$  versus  $r$ . A log-normal distribution and an exponential one are shown to guide the eye.

parabola is built with  $\hat{\mu} = 10^{-3}m$ ,  $\hat{\sigma} = 1.7$  and  $A = 3$ . While the value of  $\hat{\mu}$  is at the least very uncertain, it is clear that extrapolating the trend of the distribution leads to expect a larger value of  $r f(r)$  at smaller  $r$ . These larger values of  $r f(r)$  could be revealed by simulations with yet more refined grids than the current ones. This strongly reinforces the expectation that many smaller droplets would be seen in a true DNS. However these droplets would contribute little to the interface area. Indeed the interface area scales as

$$S = \int_0^{\infty} 4\pi r^2 f(r) dr \quad (13)$$

which for a log-normal  $f(r)$  or for a simpler  $f(r) \sim 1/r$  converges at the  $r = 0$

bound. Note that we took the assumption of spherical droplets to estimate  $S$ . The latter assumption is likely to be a good approximation for the smallest droplets. Thus the absence of the smallest droplets in the integral does not affect much the interface area  $S$ .

A simpler distribution of the form  $f(r) \sim 1/r$  would be a horizontal line in the variables of Figure 20. That approximation would not be much worse than the log-normal one in the intermediate range of droplet sizes. As a third alternative, an exponential distribution  $f(r) = A \exp(-r/r_m)$  is also plotted on Figure 20 with  $r_m = 0,02$  m. The exponential distribution is a better fit for the largest values of  $r$ . With this distribution, the interfacial area integral converges for  $\Delta x \ll r_m = 0,02$  m and thus for  $256^3$  grids. The fact that the interfacial area is seen not to converge in simulations signifies that the number of droplets is much below its theoretical level, indicating a kind of numerical “evaporation” of the droplets.

Finally we note that none of the distributions yields a very good fit. It is possible that the PDF is in fact bimodal, with different “modes” being superposed at various scales. This could be clarified by computing on even more refined grids to capture the small sizes, or using an ensemble of initial conditions as discussed below.

## 6 Summary and future work

A computational benchmark based on phase inversion of two immiscible fluids of different densities confined in a closed cubic box has been set up. The purpose of this benchmark is to check the capabilities and limitations of current codes and grid resolutions with the ultimate goal of producing numerical data of a quality similar to those provided by a DNS of single-phase turbulence. Several numerical approaches based on the one-fluid model and routinely used to compute two-phase incompressible flows have been used and compared. They include the Volume-Of-Fluid and Level-Set approaches for interface tracking, the Ghost-Fluid technique for the capture of interfacial jumps of mass and momentum, as well as several variants of Navier-Stokes solvers such as the time-splitting and augmented-Lagrangian algorithms. All these approaches and methods are *a priori* suitable for simulating the various configurations encountered in phase-inversion problems on an arbitrary grid.

The first problem we considered, case 1, is characterized by an integral scale Reynolds number  $Re = 1.37 \cdot 10^4$ . Computational results have been analyzed by considering the time evolution of several volume-averaged in-

dicators, namely the potential and kinetic energy in each fluid, the relative volume of light fluid in the top part of the box and the enstrophy in each fluid. The results reveal that all codes provide close evolutions for the first three quantities, indicating that reliable predictions are obtained when quantities essentially determined by large-scale motions are considered. The long-term decay rates of the kinetic energies have been found to be in good agreement with the viscous Stokes law (in fluid 1) and the turbulent decay law (in fluid 2) discussed in Appendix A, respectively. In addition, all codes agree on the sloshing frequency of the light fluid. The situation has been found to be much more problematic when enstrophy is considered: all codes provide markedly different values of the enstrophy maximum (although they agree on the time at which this maximum occurs) and none of them converges with respect to grid refinement.

A second phase inversion test case, involving a higher Reynolds number  $Re = 4.33 \cdot 10^5$  was subsequently considered. The same general conclusions apply to this configuration. All codes provide converging predictions as long as only kinetic and potential energies are considered, whereas large discrepancies are observed on enstrophy and interfacial area. Here again, the DNS conditions are not satisfied and much finer grids should be considered to expect convergence on quantities such as enstrophy and interfacial area which are governed by small-scale processes, especially multiple break-up events. It has to be noticed that despite the discrepancies observed on enstrophy, approximate convergence is obtained for PDFs of droplet sizes as soon as a  $1024^3$  grid is used. Clearly, case 2 is an implicit LES rather than a DNS. As a conclusion, this benchmark illustrates the fact that implicit LES simulations on fine grids allow to reach convergence on first order moments such as kinetic or potential energies while they fail to converge as soon as small scale statistics are investigated. Explicit LES models may be implemented in this case [18, 24, 34, 35, 86, 87] or finer meshes should be utilized for true DNS.

In order to disentangle physically meaningful phenomena and numerical artifacts possibly induced in the interfacial regions by the averaging rule used to define the local viscosity, complementary problems have been considered in Appendix B. They make use of the same parameters as case 1, except for viscosity  $\mu$  which is the same in both fluids and equal to 0.1, 0.01 and  $0.001 Pa.s$ . For the two largest viscosities (0.1 and  $0.01 Pa.s$ ), convergence is still not obtained for enstrophy in both fluids, but less violent excursions are observed.

Finally, a natural and important extension of this study should address the

reproducibility of the benchmark results. In the approach reported in the current paper, we do not select or force any initial interface perturbation by specifying perfectly flat interfaces located on the faces of a cube. No initial wavelength or length scale other than the size of the cube is present. Consistently with this flat character of the interface the initial velocity is zero. In an extension of this study, we have begun investigating a statistical ensemble of simulations. The ensemble is constructed by adding an interfacial or velocity perturbation at  $t = 0$ . We then perform repeatedly the same simulation with a different random perturbation each time. A statistical analysis of the problem is then performed in order to extract an average or typical flow field and interface position, and fluctuations about this average. This approach is in progress. Clearly, characterizing how simulations that are part of an ensemble with noisy or perturbed initial conditions diverge from each other is an important issue that needs to be investigated and constitutes an important perspective of extension for the present study.

Future work of all partners will first be devoted to reconsidering cases 1 and 2 on finer grids. Multiscale Eulerian VOF or Level Set approaches coupled to a Lagrangian description of small droplets will also be introduced by some of them with the goal of reaching convergence on all physical quantities on ‘reasonable’ grids that do not capture the smallest droplets. Last, adaptative mesh refinement (AMR) techniques will be considered to concentrate numerical efforts in flow regions where the vorticity magnitude is expected to reach its peak.

## 7 Acknowledgements

This work is part of the MODEMI ANR project (*Modélisation et Simulation Multi-échelle des Interfaces*, ANR-11-MONU-0011) devoted to the multiscale modeling of two-phase flows. We thus acknowledge the support of the Agence Nationale de la Recherche (ANR) for the I2M, DALEMBERT, CORIA and IMFT laboratories concerning the Multiscale Modeling of Interfaces. The authors wish to thank the Midi-Pyrénées and Aquitaine Regional Councils for the financial support dedicated to a PhD thesis at ONERA and IMFT and a 256-processor cluster investment, located in the TREFLE team of the I2M laboratory. We are grateful for access to the computational facilities of the French CINES (National computing center for higher education) and CCRT (National computing center of CEA) under project number x20142b6115, x20152b6115, x20162b6115 and A0012b06115. This work was also partly

granted access to the HPC resources of CALMIP under the allocation 2013-P0633. The CORIA team would like to express its gratitude to the CRIHAN (Centre de Ressources Informatiques de HAute-Normandie, [www.crihan.fr](http://www.crihan.fr)) computational centre used for providing CPU resources.

## A Appendix A: Scaling laws for the kinetic energy decay

After the acceleration stage induced by buoyancy forces, during which most of the lighter fluid goes to the top part of the cavity, the phase inversion problem is characterized in a second time by a wavy behavior which makes it look quite similar to a sloshing flow progressively damped by shearing and viscous effects. The classical analysis of Stokes regarding the viscous damping of gravity waves (see e.g. [88], pp. 623-624), makes it possible to predict the time evolution of the kinetic energy in a weakly viscous flow driven by a surface wave. First, the time evolution of the mechanical energy, which is the sum of the potential and kinetic energies, is known to result from the internal viscous dissipation, so that

$$\frac{dE_{mech}}{dt} = -\frac{1}{2}\mu \int_{\Omega} (\nabla \mathbf{u} + \nabla^t \mathbf{u})^2 dV \quad (14)$$

If we assume the shear layer at the free surface to have negligible effect owing to the moderate velocity gradients expected in this region, the flow can be considered as irrotational. Then the velocity potential,  $\phi$ , and mechanical energy,  $E_{mech}$ , read

$$\phi = \phi_0 e^{kz} \cos(kx - \omega t), \quad (15)$$

$$\frac{dE_{mech}}{dt} = -8\mu k^4 \int_{\Omega} \overline{\phi^2} dV, \quad (16)$$

where  $k$  and  $\omega$  are the wave number and wave frequency, respectively, and the overbar denotes the time average value. In the framework of linear wave theory, the potential and kinetic energies are equal. However the wave amplitude is not small in the present phase inversion problem. Nevertheless, as soon as most light fluid lies in the top part of the cavity, the potential energy stays almost constant, making the time variation of  $E_{mech}$  mainly governed by that of the kinetic energy. Therefore, still in the linear approximation, we can approximately write

$$\overline{E_{mech}} = \frac{1}{2}\rho \int_{\Omega} \overline{\mathbf{u}^2} dV \approx \frac{1}{2}\rho \int_{\Omega} \overline{\nabla \phi \cdot \nabla \phi} dV = \rho k^2 \int_{\Omega} \overline{\phi^2} dV \quad (17)$$

Now, two markedly different flow situations can be met in the phase inversion problem, namely a “gentle” configuration in which break-up and coalescence events of the light fluid is scarcely occur and a “violent” configuration in which such events are much more numerous. Combining (16) and (17), the time evolution of the kinetic energy in the first regime is found to obey

$$\overline{E_{mech}} = \frac{1}{2}\rho \int_{\Omega} \overline{\mathbf{u}^2} dV = K e^{-8\nu k^2 t} = K e^{-8\nu \frac{\omega^4}{g^2} t}, \quad (18)$$

where  $K$  is a constant,  $\nu = \mu/\rho$ , and use has been made of the dispersion relation  $\omega^2 = gk$ .

Let us now consider the “violent” configuration. In this case, averaging throughout the whole volume  $\Omega$ , (15)-(16) simply yields

$$\widetilde{\mathbf{u}^2} = \widetilde{\nabla\phi \cdot \nabla\phi} = k^2 \widetilde{\phi^2}, \quad (19)$$

$$\frac{d\overline{E_{mech}}}{dt} = -8\mu k^2 \widetilde{\mathbf{u}^2}, \quad (20)$$

where  $\widetilde{\cdot}$  denotes the mean value over  $\Omega$ . In other words, one has

$$\frac{d\widetilde{\mathbf{u}^2}}{dt} = -16\nu k^2 \widetilde{\mathbf{u}^2} \quad (21)$$

In this configuration, the flow is expected to be turbulent and the molecular viscosity is not relevant any more to estimate the flow damping rate. As a crude surrogate, we can introduce an effective turbulent viscosity  $\nu_t$  scaling as  $l\widetilde{\mathbf{u}}$ , where  $l$  is a characteristic length of the large-scale flow, which can be taken as the box size. Replacing  $\nu$  by  $\nu_t$  in (21), we then obtain

$$\frac{d\widetilde{\mathbf{u}^2}}{dt} = -16lk^2 \widetilde{\mathbf{u}^3} \quad (22)$$

Assuming the volume-averaged velocity to follow a power law, i.e.  $\widetilde{\mathbf{u}}$  to be of the form  $\widetilde{\mathbf{u}}_0 t^{-n}$ , immediately yields  $n = 1$ , from which we infer

$$\overline{E_{mech}} \sim t^{-2} \quad (23)$$

This prediction is to be compared with the exponential decay predicted by (18) in the “gentle” regime. The result (23) is reminiscent of the approximate decay law of decaying homogeneous isotropic turbulence (e.g. [89]). This is expected since, according to Taylor’s estimate, the dissipation rate  $\epsilon$  is known to scale as  $u_0^3/l_0$ , where  $u_0$  and  $l_0$  stand for the large-scale velocity and length scales, respectively. Therefore, when  $l_0$  is constant, (23) is immediately recovered and the dissipation rate is predicted to decay as  $t^{-3}$ .

## B Appendix B: influence of viscosity on the flow dynamics

In order to better understand the origin of code- and grid-dependences of the volume-averaged enstrophy in cases 1 and 2, we perform an extra series of computations in which the viscosity is identical in the two fluids. In this way, any possible influence of the averaging procedure selected to compute the local viscosity as a function of the volume fraction and of the numerical treatment of the viscosity jump in the interfacial grid cells is removed. We make use of the physical parameters of case 1, except for viscosity which is set to  $0.1Pa.s$  (case 1a),  $0.01Pa.s$  (case 1b) and  $0.001Pa.s$  (case 1c), respectively. The simulations are only carried out with the DyJeAT code, as it allows us to use the largest grids at a reasonable cost. The convergence study is performed on three different grids, namely  $128^3$ ,  $256^3$  and  $512^3$  in case 1a, whereas four grids ranging from  $128^3$  to  $1024^3$  are considered in cases 1b and 1c.

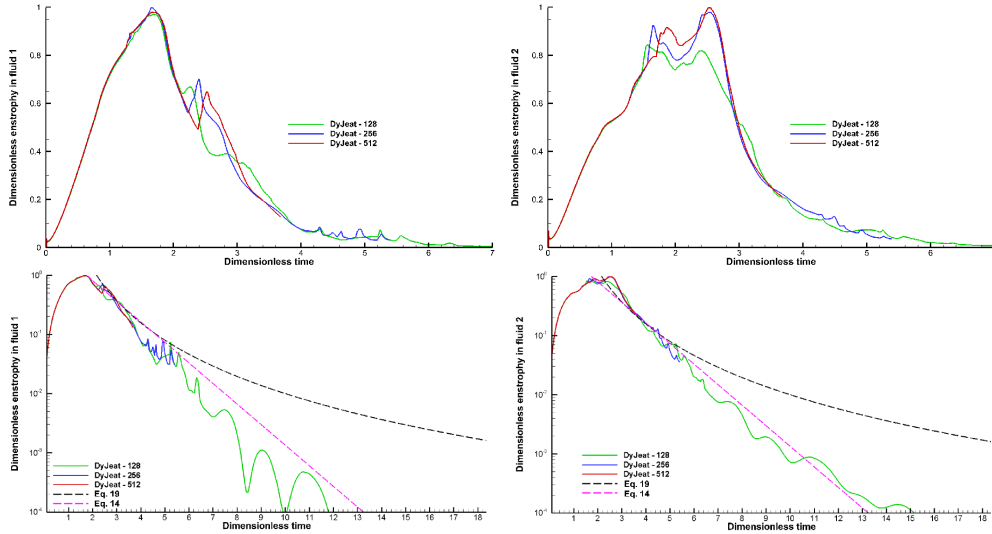


Figure 21: Grid convergence of enstrophy for case 1a in fluid 1 (left) and fluid 2 (right) - linear-linear (top) and log-linear (bottom) coordinates.

The evolution of the volume-averaged enstrophy is reported in Figures 21, 22 and 23 for cases 1a, 1b and 1c, respectively. In case 1a, the Reynolds number is 130 and the enstrophy while still not converging as the grid is further refined, has less violent excursions. In this configuration, the enstrophy decay

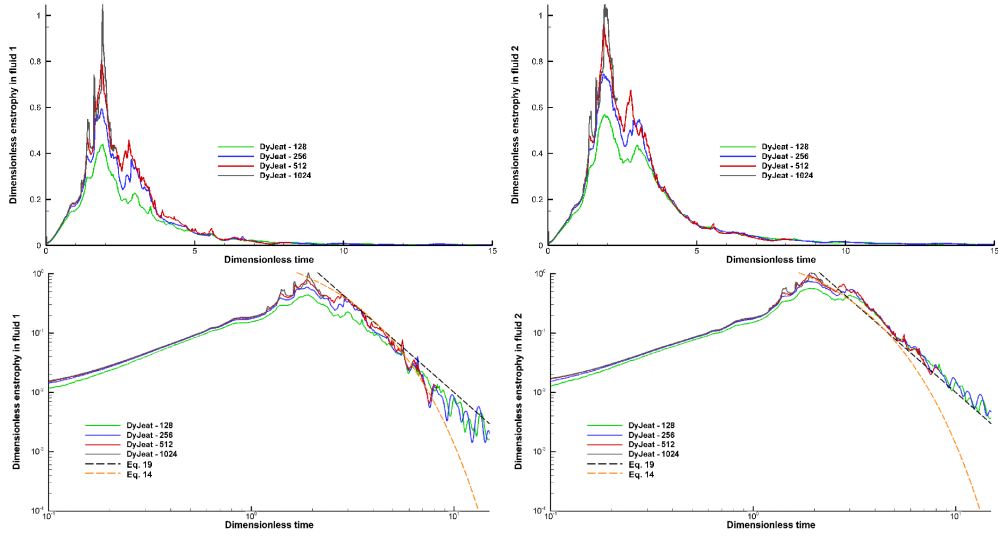


Figure 22: Grid convergence of enstrophy for case 1b in fluid 1 (left) and fluid 2 (right) - linear-linear (top) and log-log (bottom) coordinates.

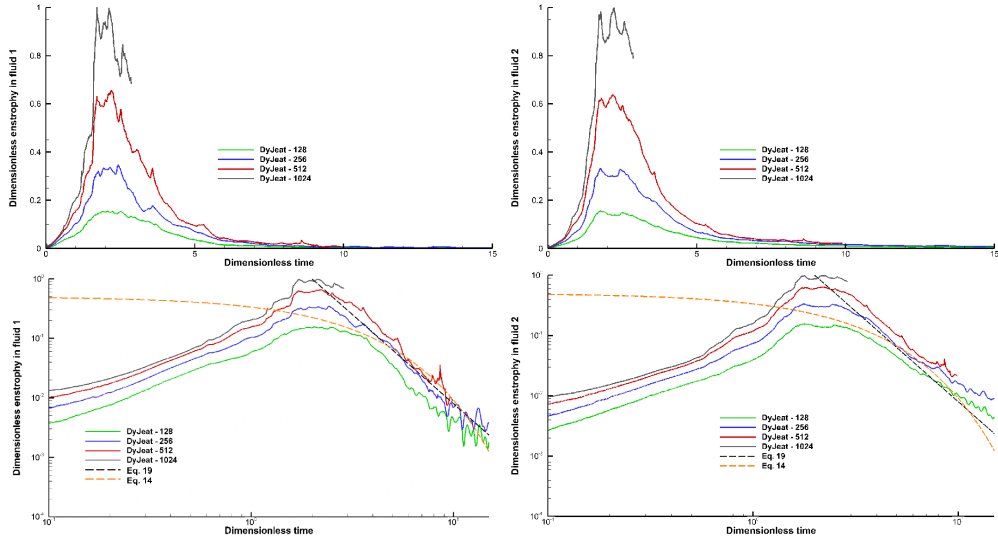


Figure 23: Grid convergence of enstrophy for case 1c in fluid 1 (left) and fluid 2 (right) - linear-linear (top) and log-log (bottom) coordinates.

at large time follows an exponential law, a behavior typical of the viscous decay of gravity waves (see appendix A). In case 1b, grid convergence is also not achieved in both fluids, the Reynolds number in fluid 2 being 1300. At large

time, the enstrophy obeys a  $t^{*-3}$  decay law typical of turbulent conditions (see appendix A). In case 1c, enstrophy convergence is not achieved in either fluid. The Reynolds number is  $1.37 \cdot 10^4$  and it is observed that, even though the results concerning energy and relative volume in the upper part of the box converge, as shown with case 1, the grid is not thin enough to capture the small-scale eddies. Again, the decay law at large times corresponds of course to turbulent conditions.

## C Appendix C: convergence of the interfacial area

A simple formula is proposed in the present work to estimate the interfacial area. It is based on the detection of the cells cut by the interface by considering the gradient of the volume of fluid. It is reported in equation (7). This estimate can be considered to be rough compared to a more accurate calculation provided by the sum of the surface of the planes generated by the VOF-PLIC method. However, the interest of (7) is that it can be utilized whatever the interface tracking algorithm (VOF or Level Set).

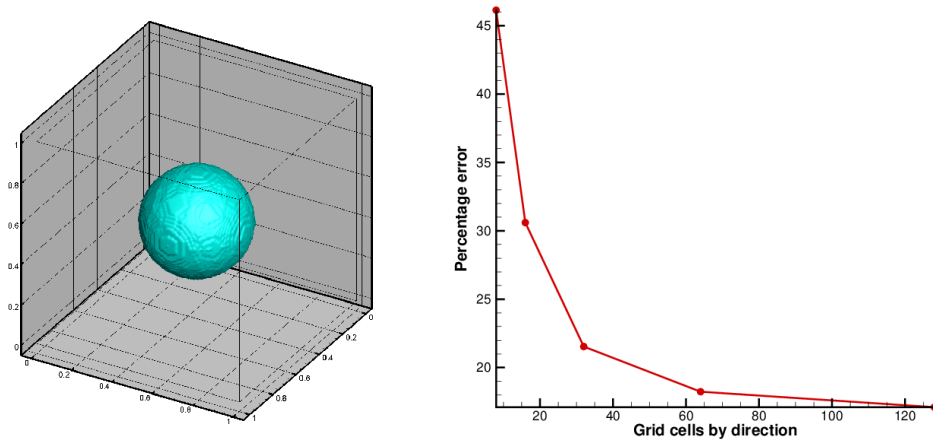


Figure 24: Convergence of formula (7) for interface area calculation - sphere surface on a  $128^3$  grid (left) and grid convergence of the interfacial area (right) compared to the exact sphere surface.

In order to evaluate the accuracy of formula (7), it is proposed to estimate the interfacial area of a sphere of radius  $0.25m$  placed in a square domain of

side size  $1m$ . The sphere surface obtained with a VOF function on a  $128^3$  grid is presented in Fig. 24 together with the convergence of the percentage error on the interfacial area with respect to grid refinement. It has to be noticed that in the present case, the exact interfacial area is  $\pi/4$ . The percentage error decreases from 50% to 18% for a number of grid cells being 8 to 128 in each Cartesian space direction. The coarser grid is representative of an under resolved drop containing 2 grid cells over a radius whereas the  $128^3$  grid is representative of a well resolved drop with 32 grid cells over a radius. These are typical characteristics that are encountered in the phase inversion simulations. It can be estimated that the error brought by (7) is belonging to the range 20% to 50% which is not so bad for a rough approximation. A better estimate is certainly provided by the sum of the surface of the planes coming from the VOF-PLIC reconstruction. An illustration is given in Fig. (18). The gap between (7) (noted Int. Modemi) and VOF PLIC calculation (noted Int. PLIC) on a  $128^3$  grid for the Gerris code is 30%, which is in agreement with the present convergence study.

## References

- [1] W.J. Rider and D.B. Kothe. Reconstructing volume tracking. *J. Comput. Phys.*, 141:112–152, 1998.
- [2] M. Rudman. A volume-tracking method for incompressible multifluid flows with large density variations. *Int. J. Numer. Meth. Fluids*, 28:357–378, 1998.
- [3] Various Authors. Test-cases for interface tracking methods. <http://test.interface.free.fr/>, 2003.
- [4] A. Benkenida and J. Magnaudet. A method for the simulation of two-phase flows without interface reconstruction. *C. R. Acad. Sci. Paris Série Iib*, 328:25–32, 2000.
- [5] S. Popinet. An accurate adaptive solver for surface-tension-driven interfacial flows. *J. Comput. Phys.*, 228:5838–5866, 2009.
- [6] A. Prosperetti. Motion of two superposed viscous fluids. *Phys. Fluids*, 24:1217, 1981.
- [7] N. Ashgriz and J.Y. Poo. Coalescence and separation in binary collisions of liquid drops. *J. Fluid Mech.*, 221:183–204, 1990.

- [8] S. Tanguy and A. Berlemont. Application of a level set method for simulation of droplet collisions. *Int. J. Multiphase Flow*, 31:1015–1035, 2005.
- [9] J.C. Martin and W.J. Moyce. An experimental study of the collapse of liquid columns on a rigid horizontal plane. *Philos. Trans. R. Soc. A-Math. Phys. Eng. Sci.*, 244:312–324, 1952.
- [10] J. Delteil, S. Vincent, A. Erriguible, and P. Subra-Paternault. Numerical investigations in Rayleigh breakup of round liquid jets with VOF methods. *Comput. Fluids*, 50:10–23, 2011.
- [11] J. C. Lasheras and E. J. Hopfinger. Liquid jet instability and atomization in a coaxial gas stream. *Annu. Rev. Fluid Mech.*, 32:275–308, 2000.
- [12] Y. Ling, D. Fuster, G. Tryggvason, and S. Zaleski. A two-phase mixing layer between parallel gas and liquid streams: multiphase turbulence statistics and influence of interfacial instability. *J. Fluid Mech.*, 859:268–307, 2019.
- [13] J. Eggers and E. Villermaux. Physics of liquid jets. *Rep. Prog. Phys.*, 71:036601, 2008.
- [14] L. Gilman and E. Baglietto. A self-consistent, physics-based boiling heat transfer modeling framework for use in computational fluid dynamics. *Int. J. Multiphase Flow*, 95:35–53, 2017.
- [15] J. Lu and G. Tryggvason. Direct numerical simulations of multifluid flows in a vertical channel undergoing topology changes. *Phys. Rev. Fluids*, 3(8):084401, 2018.
- [16] C. Josserand and S.T. Thoroddsen. Drop impact on a solid surface. *Annu. Rev. Fluid Mech.*, 48:365–391, 2016.
- [17] L. Deike, W.K. Melville, and S. Popinet. Air entrainment and bubble statistics in breaking waves. *J. Fluid Mech.*, 801:91–129, July 2016.
- [18] S. Vincent, D. Lacanette, J. Larocque, A. Toutant, P. Lubin, and P. Sagaut. Direct numerical simulation of phase separation and *a priori* two-phase LES filtering. *Comput. Fluids*, 37:898–906, 2008.
- [19] Y. Ling, D. Fuster, S. Zaleski, and G. Tryggvason. Spray formation in a quasiplanar gas–liquid mixing layer at moderate density ratios: A numerical closeup. *Phys. Rev. Fluids*, 2(1):014005, January 2017.

- [20] J.-P. Matas, A. Delon, and A. Cartellier. Shear instability of an axisymmetric air–water coaxial jet. *J. Fluid Mech.*, 843:575–600, March 2018.
- [21] M. Lance and J. Bataille. Turbulence in the liquid phase of a uniform bubbly air-water flow. *J. Fluid Mech.*, 222:95–118, 1991.
- [22] H. Chanson. Air-water flow measurements with intrusive, phase-detection probes: Can we improve their interpretation? *J. Hydraulic Eng.*, pages 252–255, 2002.
- [23] K.M.T. Kleefsman, G. Fekken, A.E.P. Veldman, B. Iwanowski, and B.A. Buchner. Volume-of-fluid based simulation method for wave impact problems. *J. Comput. Phys.*, 206:363–393, 2005.
- [24] J. Larocque, S. Vincent, P. Lubin, D. Lacanette, and J.-P. Caltagirone. Parametric study of LES subgrid terms in a turbulent phase separation flow. *Int. J. Heat Fluid Flow*, 31:536–544, 2010.
- [25] A.W. Cook, W. Cabot, and P.L. Miller. The mixing transition in Rayleigh-Taylor instability. *J. Fluid Mech.*, 511:333–362, 2004.
- [26] P. Ramaprabhu, G. Dimonte, and M.J. Andrews. A numerical study of the influence of initial perturbations on the turbulent Rayleigh-Taylor instability. *J. Fluid Mech.*, 536:285–319, 2005.
- [27] G. Boffetta, F. De Lillo, A. Mazzino, and L. Vozella. The ultimate state of thermal convection in Rayleigh-Taylor turbulence. *Physica D*, 241:137–140, 2012.
- [28] S. I. Abarzhi, A. Gorobets, and K. R. Sreenivasan. Rayleigh-Taylor turbulent mixing of immiscible, miscible and stratified fluids. *Phys. Fluid*, 17:081705:1–4, 2005.
- [29] G. Dimonte, D. L. Youngs, A. Dimits, S. Weber, M. Marinak, S. Wunsch, C. Garasi, A. Robinson, M. J. Andrews, P. Ramaprabhu, A. C. Calder, B. Fryxell, J. Biello, L. Dursi, P. MacNeice, K. Olson, P. Ricker, R. Rosner, F. Timmes, H. Tufo, Y.-N. Young, and M. Zingale. Rayleigh-Taylor turbulent mixing of immiscible, miscible and stratified fluids. *Phys. Fluid*, 16:1668–1693, 2004.
- [30] G. Tryggvason. Numerical simulations of the Rayleigh-Taylor instability. *J. Comput. Phys.*, 75:253–282, 1988.

- [31] W. Aniszewski, T. Ménard, and M. Marek. Volume of fluid (VOF) type advection methods in two-phase flow: A comparative study. *Comput. Fluids*, 97:52 – 73, 2014.
- [32] D. Jacqmin. Calculation of Two-Phase Navier-Stokes Flows Using Phase-Field Modeling. *J. Comput. Phys*, 155:96–127, 1999.
- [33] S. Vincent, J.-P. Caltagirone, and D. Jamet. Test case n°15: phase inversion in a closed box (pn, pe). *Multiphase Sci. Technol.*, 6:101–104, 2004.
- [34] W. Aniszewski, A. Boguslawski, M. Marek, and A. Tyliczszak. A new approach to sub-grid surface tension for LES of two-phase flows. *J. Comput. Phys.*, 231:7368–7397, 2012.
- [35] E. Labourasse, D. Lacanette, A. Toutant, P. Lubin, S. Vincent, O. Lebaigue, J.-P. Caltagirone, and P. Sagaut. Towards large eddy simulation of isothermal two-phase flows: Governing equations and *a priori* tests. *Int. J. Multiphase Flow*, 33:1–39, 2007.
- [36] R. Lebas, T. Ménard, P.A. Beau, A. Berlemont, and F.X. Demoulin. Numerical simulation of primary break-up and atomization: DNS and modelling study. *Int. J. Multiphase Flow*, 35:247–260, 2009.
- [37] G. Tomar, D. Fuster, S. Zaleski, and S. Popinet. Multiscale simulations of primary atomization. *Comput. Fluids*, 39:1864–1874, 2010.
- [38] I. Calmet and J. Magnaudet. High-schmidt number mass transfer through turbulent gas-liquid interfaces. *Int. J. Heat Fluid Flow*, 19:522–532, 1998.
- [39] S. Banerjee, D. Lakehal, and M. Fulgosi. Surface divergence models for scalar exchange between turbulent streams. *Int. J. Multiphase Flow*, 30:963–977, 2004.
- [40] J.M. Delhay. Jump conditions and entropy sources in two-phase systems. Local instant formulation. *Int. J. Multiphase Flow*, 1:395–409, 1974.
- [41] R. Scardovelli and S. Zaleski. Direct numerical simulation of free-surface and interfacial flow. *Annu. Rev. Fluid Mech.*, 31:567–603, 1999.
- [42] J.U. Brackbill, D.B. Kothe, and C. Zemach. A continuum method for modeling surface tension. *J. Comput. Phys.*, 100:335–354, 1992.

- [43] S. Osher and R. Fedkiw. Level set methods: An overview and some recent results. *J. Comput. Phys.*, 169:463–502, 2001.
- [44] S. Patankar. *Numerical heat transfer and fluid flow*. CRC Press, 1980.
- [45] A. Poux, S. Glockner, and M. Azaïez. Improvements on open and traction boundary conditions for Navier-Stokes time-splitting methods. *J. Comput. Phys.*, 230:4011–4027, 2011.
- [46] S. Vincent, A. Sarthou, J.-P. Caltagirone, F. Sonilhac, P. Février, C. Mignot, and G. Pianet. Augmented Lagrangian and penalty methods for the simulation of two-phase flows interacting with moving solids. Application to hydroplaning flows interacting with real tire tread patterns. *J. Comput. Phys.*, 230:956–983, 2011.
- [47] F. Bertrand, P.A. Tanguy, and F. Thibault. A three-dimensional fictitious domain method for incompressible fluid flow problems. *Int. J. Numer. Meth. Fluids*, 25:719–736, 1997.
- [48] M. Fortin and R. Glowinski. *Méthodes de lagrangien augmenté. Application à la résolution numérique de problèmes aux limites*. Dunod, Paris, 1982.
- [49] O. Schenk and K. Gärtner. Solving unsymmetric sparse systems of linear equations with PARDISO. *Fut. Gener. Comput. Syst.*, 20:475–487, 2004.
- [50] R.H. A. Van Der Vorst. BiCGSTAB: a fast and smoothly converging variant of BiCG for the solution of non-symmetric linear systems. *J. Sci. Comput.*, 13:631–644, 1992.
- [51] D.L. Youngs. *Time-dependent multimaterial flow with large fluid distortion*. K.W. Morton and M.J. Baines eds., Numerical Methods for Fluid Dynamics, Academic, New-York, 1982.
- [52] S. Vincent, G. Balmigère, J.-P. Caltagirone, and E. Meillot. Eulerian-Lagrangian multiscale methods for solving scalar equations - Application to incompressible two-phase flows. *J. Comput. Phys.*, 229:73–106, 2010.
- [53] T.N. Randrianarivelo, G. Pianet, S. Vincent, and J.-P. Caltagirone. Numerical modelling of the solid particle motion using a new penalty method. *Int. J. Numer. Meth. Fluids*, 47:1245–1251, 2005.
- [54] S. Vincent, T. Randrianarivelo, G. Pianet, and J.P. Caltagirone. Local penalty methods for flows interacting with moving solids at high Reynolds numbers. *Comput. Fluids*, 36:902–913, 2007.

- [55] E. Aulisa, S. Manservigi, R. Scardovelli, and S. Zaleski. Interface reconstruction with least-squares fit and split advection in three-dimensional Cartesian geometry. *J. Comput. Phys.*, 225:2301–2319, 2007.
- [56] J. Li. Calcul d’interface affine par morceaux (piecewise linear interface calculation). *C. R. Acad. Sci. Paris Série IIb*, 320:391–396, 1995.
- [57] R. Scardovelli and S. Zaleski. Interface reconstruction with least-square fit and split Lagrangian-Eulerian advection. *Int J. Numer. Meth. Fluids*, 41:251–274, 2003.
- [58] E. Aulisa, S. Manservigi, R. Scardovelli, and S. Zaleski. A geometrical area-preserving volume of fluid advection method. *J. Comput. Phys.*, 192:355–364, 2003.
- [59] G. Tryggvason, R. Scardovelli, and S. Zaleski. Direct numerical simulations of gas-liquid multiphase flows. *Cambridge University Press*, 2011.
- [60] M.M. Francois, S.J. Cummins, E.D. Dendy, D.B. Kothe, J.M. Sicilian, and M.W. Williams. A balanced-force algorithm for continuous and sharp interfacial surface tension models within a volume tracking framework. *J. Comput. Phys.*, 213:141–173, 2006.
- [61] Y. Renardy and M. Renardy. PROST: A parabolic reconstruction of surface tension for the volume-of-fluid method. *J. Comput. Phys.*, 183:400–421, 2002.
- [62] S. Popinet. Numerical models of surface tension. *Annu. Rev. Fluid Mech.*, 50:49–75, 2018.
- [63] D. Fuster, J.-Ph. Matas, S. Marty, S. Popinet, J. Hoepffner, A. Cartel-lier, and S. Zaleski. Instability regimes in the primary breakup region of planar coflowing sheets. *J. Fluid Mech.*, 736:150–176, 2013.
- [64] D. Fuster, A. Bagué, T. Boeck, L. Le Moyne, A. Leboissetier, S. Popinet, P. Ray, R. Scardovelli, and S. Zaleski. Simulation of primary atomization with an octree adaptive mesh refinement and VOF method. *Int. J. Multiphase Flow*, 35:550–565, 2009.
- [65] D. Fuster, G. Agbaglah, C. Josserand, S. Popinet, and S. Zaleski. Numerical simulation of droplets, bubbles and waves: state of the art. *Fluid Dyn. Res.*, 41:065001, 2009.

- [66] T. Bonometti and J. Magnaudet. An interface-capturing method for incompressible two-phase flows. validation and application to bubble dynamics. *Int. J. Multiphase Flow*, 33:109–133, 2007.
- [67] B. Duret, J. Reveillon, T. Menard, and F.X. Demoulin. Improving primary atomization modeling through DNS of two-phase flows. *Int. J. Multiphase Flow*, 55:130 – 137, 2013.
- [68] Chi-Wang Shu. *Essentially Non-Oscillatory and Weighted Essentially Non-Oscillatory Schemes for Hyperbolic Conservation Laws*. NASA (as NASA/CR-97-206253 report), 1997.
- [69] M. Sussman, E. Fatemi, P. Smereka, and S. Osher. Improved level set method for incompressible two-phase flows. *Comput. Fluids*, 27:663–680, 1998.
- [70] M. Sussman and E.G. Puckett. A coupled level set and volume-of-fluid method for computing 3d and axisymmetric incompressible two-phase flows. *J. Comput. Phys.*, 162:301–337, 2000.
- [71] M. Kang, R.P. Fedkiw, and X.D. Liu. A boundary condition capturing method for multiphase incompressible flow. *J. Sci. Comput.*, 15:323–360, 2000.
- [72] X.D. Liu, R.P. Fedkiw, and M. Kang. A boundary condition capturing method for poisson equation on irregular domains. *J. Comput. Phys.*, 260:151–178, 2000.
- [73] J. D. Towers. Finite difference methods for approximating heaviside functions. *J. Comput. Phys.*, 228:3478–3489, 2009.
- [74] A.J. Chorin. Numerical solution of the Navier-Stokes equations. *Math. Comput.*, 22:745–762, 1968.
- [75] R. Temam. Sur l’approximation de la solution des équations de Navier-Stokes par la méthode des pas fractionnaires. *Arch. Ration. Mech. Anal.*, 33:377–385, 1969.
- [76] R. Fedkiw, T. Aslam, B. Merriman, and S. Osher. A non-oscillatory Eulerian approach to interfaces in multimaterials flows (the ghost fluid method). *J. Comput. Phys.*, 152:457–492, 1999.
- [77] D. Zuzio and J.-L. Estivalezes. An efficient block parallel AMR method for two phase flow simulations. *Comput. Fluids*, 44:339–357, 2011.

- [78] D. Zuzio, J.-L. Estivalèzes, and B. DiPierro. An improved multi-scale Eulerian-Lagrangian method for simulation of atomization process. *Comput. Fluids*, 176:285–301, 2018.
- [79] S.A. Orszag. Analytical theories of turbulence. *J. Fluid Mech.*, 41:363–386, 1970.
- [80] P.K. Yeung and S.B. Pope. Lagrangian statistics from direct numerical simulations of isotropic turbulence. *J. Fluid Mech.*, 207:531–586, 1989.
- [81] J.-B. Ritz and J.P. Caltagirone. A numerical continuous model for the hydrodynamics of fluid particle systems. *Int. J. Numer. Meth. Fluids*, 30:1067–1090, 1999.
- [82] G. Pianet, S. Vincent, J. Leboi, J.P. Caltagirone, and M. Anderhuber. Simulating compressible gas bubbles with a smooth volume tracking 1-Fluid method. *Int. J. Mult. Flow*, 36:273–283, 2010.
- [83] S. Vincent, J.C. Brandle de Motta, A. Sarthou, J.-L. Estivalèzes, O. Simonin, and E. Climent. A Lagrangian VOF tensorial penalty method for the DNS of resolved particle-laden flows. *J. Comput. Phys*, 256:582–614, 2014.
- [84] T. Sayadi, V. Le Chenadec, S. Zaleski, and S. Popinet. A convergence study of the one-fluid formulation in a phase inversion application at moderate Reynolds and Weber numbers. *to be published in Notes Numer. Fluid Mech. Multidisciplinary Design*, 2019.
- [85] M. Herrmann. On simulating primary atomization using the refined level set grid method. *Atomization and Sprays*, 21(4):283–301, 2011.
- [86] S. Vincent, M. Tavares, S. Fleau, S. Mimouni, M. Ould-Rouiss, and J.-L. Estivalèzes. A priori filtering and LES modeling of turbulent two-phase flows - application to phase separation. *Comput. Fluids*, 176:245–259, 2018.
- [87] M. Saeedipour, S. Vincent, and S. Pirker. Large eddy simulation of turbulent interfacial flows using approximate deconvolution model. *Int. J. Multiphase Flow*, 112:286–299, 2019.
- [88] H. Lamb. *Hydrodynamics*. Cambridge University Press, 1932.
- [89] P. Sagaut and C. Cambon. Homogeneous turbulence dynamics. *Cambridge University Press*, 2008.